

Review

Theory and Practices of Li-Ion Battery Thermal Management for Electric and Hybrid Electric Vehicles

Rajib Mahamud ¹  and Chanwoo Park ^{2,*} 

¹ Department of Mechanical Engineering, Idaho State University, Pocatello, ID 83201, USA; rajibmahamud@isu.edu

² Department of Mechanical Engineering, University of Missouri, Columbia, MO 65211, USA

* Correspondence: parkchanw@missouri.edu

Abstract: This article surveys the mathematical principles essential for understanding the thermal management of Li-ion batteries, the current technological state of the art, and the solution. Since the thermal management of electric drive vehicles has environmental, economic, and safety impacts, this review focuses on the efficient methods of battery thermal management (BTM) that were proposed to overcome the major challenges in the electric vehicle industry. The first section examines the perspective of battery-driven vehicles, the principles of Li-ion batteries with a thermal runaway, and their implication for battery safety. The second section discusses mathematical approaches for effective BTM modeling, including the thermal-fluidic network model, lumped capacitance model, spatial resolution lumped capacitance model, equivalent circuit model, impedance-based model, and data-driven model. The third section presents the current state-of-the-art technologies, including air-based, liquid-based, PCM-based, in situ BTM methods, and heat pipe and thermoelectric module-based methods. The conclusion section summarizes the findings from existing research and the possible future directions to achieve and employ better thermal management techniques.

Keywords: Li-ion; battery thermal management; modeling; air and liquid cooling; heat pipe; phase change materials; in situ methods



Citation: Mahamud, R.; Park, C. Theory and Practices of Li-Ion Battery Thermal Management for Electric and Hybrid Electric Vehicles. *Energies* **2022**, *15*, 3930. <https://doi.org/10.3390/en15113930>

Academic Editor: Michel L. Trudeau

Received: 25 March 2022

Accepted: 20 May 2022

Published: 26 May 2022

Publisher's Note: MDPI stays neutral with regard to jurisdictional claims in published maps and institutional affiliations.



Copyright: © 2022 by the authors. Licensee MDPI, Basel, Switzerland. This article is an open access article distributed under the terms and conditions of the Creative Commons Attribution (CC BY) license (<https://creativecommons.org/licenses/by/4.0/>).

1. Introduction

After an era (nearly a hundred years) of vehicles driven by internal combustion engines, electric vehicles have finally become the choice of automotive technology in recent years. Electric vehicles have recently garnered considerable interest because of their economic, environmental, and social impacts. They are considered one of the pillars of sustainable development and green transformation and can be combined with other renewable energy technologies [1–5]. An advanced battery system can support electric vehicles as well as several other applications, including portable electronics, energy storage applications, solar or wind energy storage and utilization, and marine vehicle applications. Hence, there has been an increasing demand for advanced batteries and battery management systems to ensure the efficient performance and long lifetime of electric vehicles by maintaining an appropriate battery temperature during extreme environments and weather events. To tackle these challenges, the major research effort has been directed toward the development of new types of electrode materials, focusing on achieving high heat capacity and the prevention of short circuits that lead to thermal runaway. Efficient thermal management is crucial to achieving a profit-maximization paradigm, where the potential side effects from the development of a high-energy cell and thermal runaway situations can be minimized. An advanced battery system should be developed based on innovative approaches to find generalized multi-purpose solutions; however, such a system has not been realized, and multidisciplinary efforts should be made to resolve the current challenges while supporting sustainability. In this regard, a Li-ion battery is not fully sustainable. It has been recognized

that environmental challenges are associated with material mining and recycling, and research efforts have been made to address the problems in all sectors. Approaches to address the problems in the thermal management performances of Li-ion batteries have also been proposed; it is believed that improving the thermal management performance can solve many problems associated with the development of electric vehicles and related technologies.

A Li-ion battery is a primary option for electric and hybrid electric vehicles because it offers certain major advantages. The lowest reduction potential of this battery among those of other alternatives renders it as having the highest possible cell potential. Moreover, Li is the third-lightest element, and the radius of Li-ion is the smallest among the radii of single charged ions; therefore, Li-ion batteries possess the highest volumetric and gravimetric capacities and power density. However, the commercialization of Li-ion battery entails scale up design from the material to the cell and the battery pack and relies on cost, energy, power, weight, and volumetric requirements as envisioned in Figure 1a,b [3].

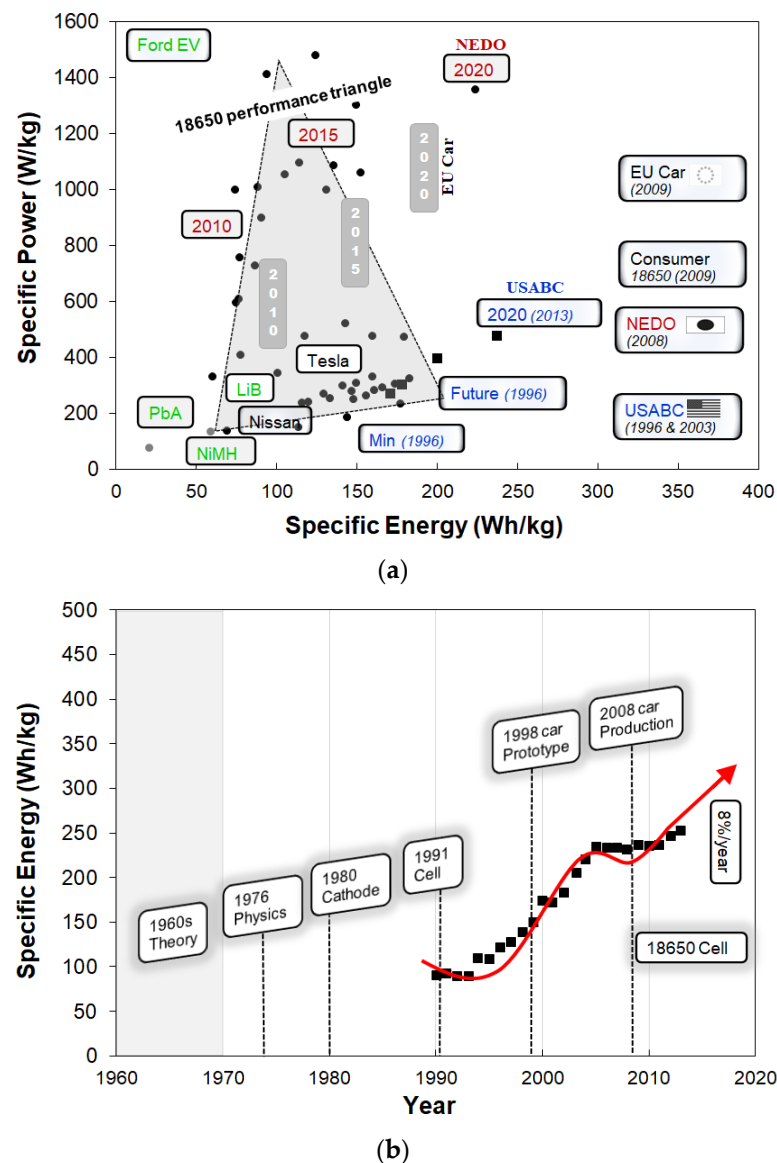


Figure 1. (a) EVs and 18650 cell power vs. energy for some commercially available cells under different applications. Adapted with permission from [3]. Copyright 2003 Springer. (b) Increase in specific energy of 18650 Li cell thanks to the development over the last 50 years when the intercalation/deintercalation of Li was shown. Adapted with permission from [3]. Copyright 2018 Springer.

Considering the leverage between these multifaceted factors in EVs and HEVs, a performance diagram can be portrayed focusing on optimization of specific power vs specific energy (Figure 1a) as shown for the state of the art 18650 cell. It is evident that the performance of Nissan (Leaf), Ford, and Tesla (Model S) fit inside the 18650-performance triangle. Figure 1a also depicts the performance target of some of the organizations including United States Advanced Battery Consortium (USABC), the European Council for Automotive Research and Development (EUCAR), and the New Energy and Industrial Technology Development Organization (NEDO) [3].

In retrospect, the intercalation/deintercalation of Li-ion was first demonstrated in 1960 [6]; since then, several advancements in the research of Li-ion batteries have been made over the past 50 years (Figure 1b), focusing on the development of anode/cathode and electrolyte materials and efficient charge-transfer technologies. Li-ion cells store energy (electrical) in cathode-containing Li compounds that are capable of reversible intercalation of Li ions; the energy is also stored in negative electrode materials that usually include graphite or carbon, which accommodates solid-state Lithium (Figure 2). Sony Corporation developed the first cell (size 18650), which instantly became popular in small-scale electronics markets. The practicality of the Li-ion cell was based on a few key solving steps. The first is the adoption of LiCoO_2 as a cathode, as proposed by Mizushima [7] and Goodenough [8], which is the most commonly used cathode material. The most common anode material is graphite, followed by propylene carbonate, which has a greater capacity than that of graphene and does not cause the decomposition of the propylene carbonate electrolyte solvent. Electrolytes are blends of ionizable organic solvents, for example, propylene carbonate, and suitable lithium salts. Another important part of battery development is a multilayer electrode assembly, fabricated by winding cathode/anode sheets and by placing a membrane (separator) betwixt and between, which is inserted into the cell; subsequently, a nonaqueous electrolyte solution, such as LiPF_6 or LiBF_4 , is infused, and a mixture of carbonate compounds is added; the resultant mixture is then sealed in a can. Another notable advancement was the development of highly functional membrane separators, such as ceramic particle-coated microporous polyethylene films. The separator, such as a microporous polyethylene membrane with a thickness of 20–30 μm , performs a shutdown function in the case of abnormal heat generation; the material of the separator melts to close the micropores and cease the cell operation. To address such an issue of abnormal heat generation, the anode material can be coated with Al_2O_3 . These newly developed separators can increase the fire safety and stability of the cell. New technologies are required for the improvement of battery performance and sustainability while considering the energy density and safety characteristics. Some of these recent technological developments include organic positive electrodes that eliminate the requirements of expensive metal, positive electrodes with lithium for realizing a large discharge capacity, and ceramic-coated separators that provide excellent thermal stability and do not cause an internal short circuit when charged to 43 V and heated up to 150 °C [9–12].

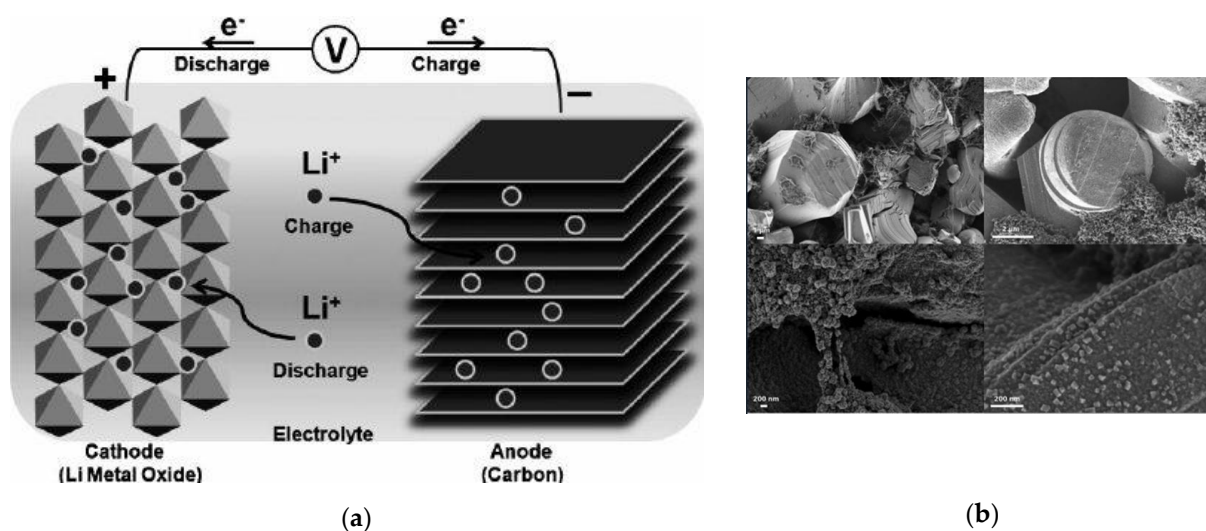


Figure 2. (a) A schematic diagram depicting the process and chemistry of a Li-ion cell [4,13]. Reprinted with permission from [13]. Copyright 2009 Wiley. (b) Scanning electron microscopy of cathode, anode, binder, and separator [14]. Reprinted from an open access blog [14].

Safety is a critical consideration for developing Li-ion cells owing to their high power density and flammable electrolytes [15,16]. Thermal runaway [17], which starts as a chain reaction, is a major safety issue and depends on the anode and cathode materials, electrolytes, and reactions during battery operation (Table 1). A rapid increase in incidents and injuries due to the thermal runaway has been reported over the years. Thermal runaway occurs due to several reasons, such as a collision or damage causing penetration of the cell; external or internal short-circuits; overcharging, which causes excessive lithium intercalation at the anode or excessive de-intercalation at the cathode; over-discharge, which causes capacity degradation due to the over-delithiation in the anode as well as amorphization in the cathode, and intensive heat generation caused by the passing of high current through a given area, resulting in local overheating (Figure 3). To prevent thermal runaway, the cathode can be coated with thermally and chemically inert materials, such as phosphate, fluoride, and solid oxide; alternatively, $\text{Li}(\text{Ni}_{0.4}\text{Mn}_{0.33}\text{Co}_{0.13}\text{Al}_{0.13})\text{O}_2$ can be used as the cathode material to achieve high thermal stability [18]. In addition, a graphite anode can be coated with Al_2O_3 [19]. Furthermore, new anode materials such as $\text{Li}_4\text{Ti}_5\text{O}_{12}$ (LTO) and alloys have been studied to enhance the safety of Li-ion cells [20]. Similarly, several electrolytes have been considered to test the thermal stability of the cell; these electrolytes include inflammable organic carbonate solvents, flame retarded additives, and imide-based lithium salts.

Having discussed some of the approaches for mitigating thermal runaway, we now focus on thermal management to prevent any abnormal temperature rise or thermal runaway conditions that can cause severe fire hazards. The operating temperature range of a cell depends on the materials used; for example, Li-ion or NiMH batteries operate best when the operating temperature is within 25–40 °C and exhibit a stable balance between performance and life. It should be noted that the operation at low temperatures can be inefficient due to the high internal electrical resistance and slow electrochemical reaction rates. At a very low ambient temperature, chemical reactions are primarily braked by slower diffusion rates and Li-plating—Li metal deposition at the anode [21,22]. These phenomena are more pronounced in cold climates and during a cold start, affecting both the power density and the energy density of the cells.

Table 1. Reactions relevant to Li-ion battery thermal runaway [15,16]. Copyright 2012 Elsevier.

Reactions	Reaction Chemistry	Temperature (°C)
SEI decomposition	$(\text{CH}_2\text{OCO}_2\text{Li})_2 \rightarrow \text{Li}_2\text{CO}_3 + \text{C}_2\text{H}_4 + \text{CO}_2 + 0.5\text{O}_2$	90–120
Negative electrode/electrolyte	$2\text{Li} + \text{C}_3\text{H}_4\text{O}_3 \text{ (EC)} \rightarrow \text{Li}_2\text{CO}_3 + \text{C}_2\text{H}_4$	>100
	$2\text{Li} + \text{C}_4\text{H}_6\text{O}_3 \text{ (PC)} \rightarrow \text{Li}_2\text{CO}_3 + \text{C}_3\text{H}_6$	
	$2\text{Li} + \text{C}_3\text{H}_6\text{O}_3 \text{ (DMC)} \rightarrow \text{Li}_2\text{CO}_3 + \text{C}_2\text{H}_6$	
Separator meltdown	-	~130
Positive electrode decomposition	$\text{Li}_x\text{CoO}_2 \rightarrow x\text{LiCO}_2 + 1/3(1-x)\text{Co}_3\text{O}_4 + 1/3(1-x)\text{O}_2$	196–230
	$\text{Co}_3\text{O}_4 \rightarrow 3\text{CoO} + 0.5\text{O}_2$	
	$\text{CoO} \rightarrow \text{Co} + 0.5\text{O}_2$	
Solvent/O ₂	$2.5\text{O}_2 + \text{C}_3\text{H}_4\text{O}_3 \text{ (EC)} \rightarrow 3\text{CO}_2 + 2\text{H}_2\text{O}$	
	$4\text{O}_2 + \text{C}_4\text{H}_6\text{O}_3 \text{ (PC)} \rightarrow 4\text{CO}_2 + 3\text{H}_2\text{O}$	
	$3\text{O}_2 + \text{C}_3\text{H}_6\text{O}_3 \text{ (DMC)} \rightarrow 3\text{CO}_2 + 3\text{H}_2\text{O}$	
Electrolyte decomposition	$\text{LiPF}_6 \rightarrow \text{LiF} + \text{PF}_5$	200–300
	$\text{C}_2\text{H}_5\text{OCOOPF}_4 \rightarrow \text{PF}_3\text{O} + \text{CO}_2 + \text{C}_2\text{H}_4 + \text{HF}$	
Positive electrode/electrolyte	$2\text{Li} + 2\text{EC} \rightarrow \text{Li-O-(CH}_2)_4\text{-O-Li} + 2\text{CO}_3$	200–240
	$\text{Li-O-(CH}_2)_4\text{-O-Li} + \text{PF}_5 \rightarrow \text{Li-O-(CH}_2)_4\text{-F} + 2\text{LiF} + \text{POF}_3$	
Negative electrode/binder	$-\text{CH}_2\text{-CF}_2 + \text{Li} \rightarrow \text{LiF} + \text{-CH}=\text{CF} + 0.5\text{H}_2$	>260

Reprinted with permission from [15].

A battery pack contains an assembly of several series or parallelly connected cells, and thermal instability in any of the cells can cause a chain reaction in the pack, resulting in an explosion and fire. Thermal instability in any cell can be initiated by non-uniform cooling in the pack and non-uniform heat generation in the cell, particularly at a higher discharge current. In such cases, the heat generation in a cell varies significantly in the radial (spiral) direction from the terminal (core) to the battery skin (surface). At higher discharge currents, the current discharge is significantly higher in the terminal and lower at the surface [23]. This condition resembles a high Biot number condition in a very large cell, where the core temperature is significantly larger than the surface temperature. Therefore, BTM is crucial to keep the cell temperature in an operational temperature range and maintain a uniform temperature between cells, thus preventing them from locally overheating. Conversely, cell performance at very low and subzero temperatures is degraded by slower electrochemical responses and Li-plating [24–26]. Thereby, thermal management cannot be practically realized without both cooling and heating functions depending on different weather conditions.

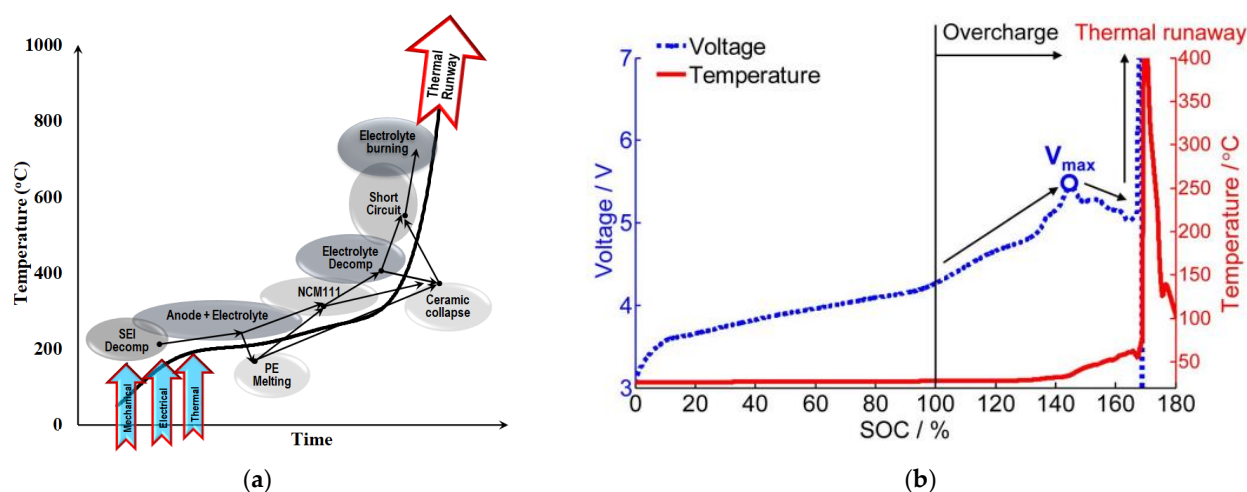


Figure 3. (a) Qualitative interpretation of the chain reactions during thermal runaway. (b) Overcharge induced thermal runaway for a commercial lithium-ion battery [27]. Adapted with permission from [17,27]. Copyrights 2020 Elsevier.

A comparison of primary cell types is presented in Figure 4 in terms of cell construction, materials, and key performance parameters of Li-ion cells: energy density, cost/kWh, and thermal performance. The form factor (coin, cylindrical, prismatic, and pouch) of a battery cell greatly affects the thermal performance and packaging designs of battery systems. Cylindrical cells of 18650 and 21700 are the primary choices for EVs and HEVs due to their superior thermal performance. Note that the first two numbers (18 and 21) refer to the diameter of the cell in millimeters, the next two numbers (65 and 70) stand for the height of the cell in millimeters, and the fifth number (0) means the cylindrical form factor. In contrast, coin, prismatic, or pouch cells are easily adaptable in electronics applications due to fewer packaging constraints [28–31]. The cylindrical 18650 cells have a higher energy density and a slightly higher cost/kWh than the prismatic or pouch cells. The recent cylindrical 21700 cells significantly reduce the cost/kWh with a ~50% higher energy content than the 18650 cells [32]. Regarding thermal performance, cylindrical cells provide a better heat transfer due to more uniform cell temperature, higher surface area to volume ratio, and inherent gaps between the cells than the prismatic or pouch cells. Hence, in the remainder of the review, we will discuss the recent advancement of mathematical and numerical modeling and thermal management practices, primarily focusing on the cylindrical cell type in either individual or system/pack level configurations.

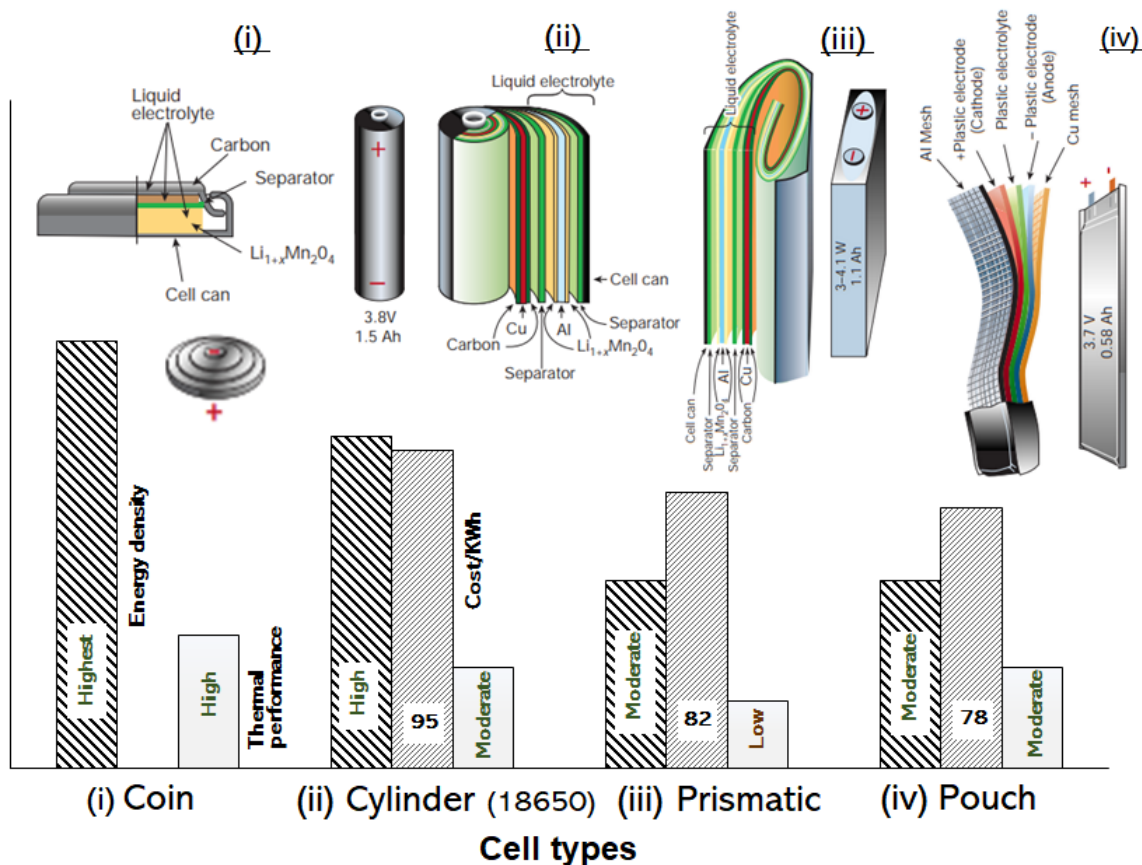


Figure 4. Comparison of key performance parameters of Li-ion cells of primary cell types [33,34] showing cell construction and materials [35]. Adapted with permission from [35]. Copyright 2001 Nature.

2. Modeling of Battery Thermal Management System

The modeling of the BTMS are discussed in this section are standard lumped-capacitance (LC) thermal model with flow network model for a pack level system [36,37], spatial resolution lumped-capacitance thermal model for a cell level understanding of battery

system [38,39], equivalent circuit model [40–42], impedance-based model [43,44], and data-driven model [45,46].

2.1. Lumped-Capacitance Thermal Model and Flow Network Model

Li-ion batteries come in two main form factors: prismatic and cylindrical. The cylindrical type is more common than the prismatic type, and it is usually constructed in a multilayer spiral structure assembled radially, resulting in a lower effective thermal conductivity that dominates heat conduction compared to axial conduction. However, the thermal resistance due to the radial conduction is much less than convective thermal resistance; hence, the Biot number is significantly less than 1. Therefore, most numerical studies have employed the standard lumped-capacitance thermal model supposing an even temperature in the cell from the core to the surface. This assumption allows using transient thermal boundary conditions, simulating an actual duty cycle and real-time battery control, while reducing the computational load and time.

A test module comprising eight cells (yellow circles in Figure 5a) with symmetric boundary conditions on both its sides was modeled using the LC thermal model and a flow network model. Figure 5b,c depict the thermal circuit diagram of a cell and the eight-cell module [12].

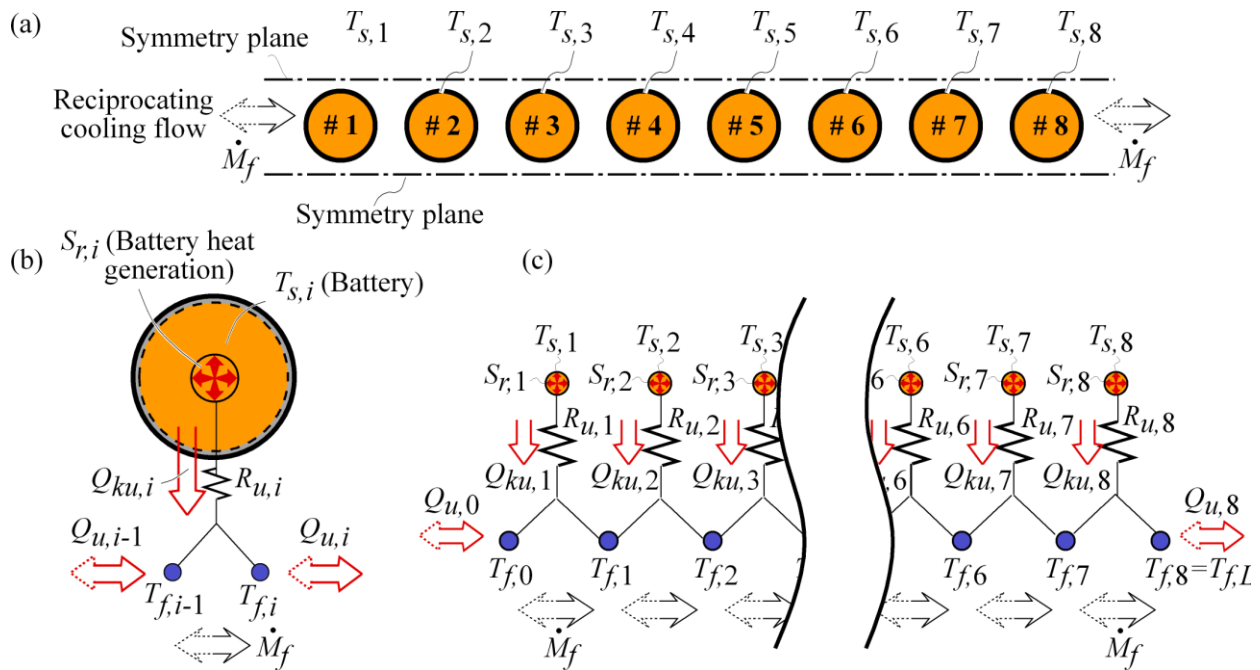


Figure 5. (a) A schematic diagram of the eight-cell thermal circuit, (b) single-cell thermal circuit, and (c) flow network model. Reprinted with permission from [36]. Copyrights 2011 Elsevier.

Applying the first law of thermodynamics for an individual cell (index number i)

$$(\rho c_p V)_{s,i} \frac{dT_{s,i}}{dt} = S_{r,i} - Q_{ku,i} \tag{1}$$

where $S_{r,i}$ is the heat generation rate in a cell. The $S_{r,i}$ in a cell is modeled as the summation of the (i) Joule (irreversible) and (ii) entropic (reversible) heats and is expressed by

$$S_{r,i} = Q_{irr} + Q_{rev} \tag{2}$$

where the Q_{irr} is heat generation owing to the Joule heating corresponding to the intrinsic electrical resistance R_e and is written by

$$Q_{irr} = I(E_{oc} - E) = I^2 R_e \quad (3)$$

where R_e is the internal electrical resistance of a cell and is comprehensively studied in the literature for different types of cells. In the aforementioned expression, the contribution of the electrode side reaction, such as corrosion and parasitic reactions are typically ignored. Empirical correlations for R_e are available as a function of SOC and temperature or as an average of the state-of-charge (SOC) and temperatures and is written as [36,47]

$$R_e = -0.0001 T^3 + 0.0134 T^2 - 0.5345 T + 12.407 \quad (4)$$

where R_e is the internal electrical resistance in $m\Omega$ and T is the cell temperature in $^{\circ}C$.

Depending on cell types, empirical data are also available for different cell chemistries. For example, for a 2.2 Ah LiFePO₄ cell, the electrical resistance was evaluated in terms of average cell temperature and SOC [48] as below

$$R_e = 27.54 - 27.68 \exp\left(-\frac{1.91}{T}\right) + \frac{223.71}{1 + 21.1 \text{ SOC}} - \frac{225.06 \exp\left(-\frac{1.91}{T}\right)}{1 + 21.61 \text{ SOC}} \quad (5)$$

where T is the cell temperature in K and SOC is the estimated state of the charge. Likewise, the electrical resistance was also evaluated in terms of the SOC for different cell temperatures for a cylindrical SONY-US50G3 battery [49] as below

$$R_e = \begin{cases} 2.258 \times 10^{-6} \text{ SOC}^{-0.3952}, & T = 293 \text{ K} \\ 1.857 \times 10^{-6} \text{ SOC}^{-0.2787}, & T = 303 \text{ K} \\ 1.659 \times 10^{-6} \text{ SOC}^{-0.1692}, & T = 313 \text{ K} \end{cases} \quad (6)$$

The electrical resistance varies with thermal or chemical non-equilibrium, making it a function of SOC and temperature [50]. It also depends strongly on the technique and condition used for the estimation. Therefore, a predictable and reliable estimation of the battery resistance is essential in designing and evaluating battery thermal management [51]. Table 2 comprises some literature expressions of internal electrical resistance.

Table 2. Expressions of internal electrical resistance in the literature.

Cell Type	Expression or Value	Ref.
LiMn ₂ O ₄ cylindrical	$R_e = -0.0001 T^3 + 0.0134 T^2 - 0.5345 T + 12.407$	[36]
2.2 Ah LiFePO ₄ cell cylindrical	$R_e = 27.54 - 27.68 \exp\left(-\frac{1.91}{T}\right) + \frac{223.71}{1 + 21.1 \text{ SOC}} - \frac{225.06 \exp\left(-\frac{1.91}{T}\right)}{1 + 21.61 \text{ SOC}}$	[48]
SONY-US50G3 cylindrical	$R_e = \begin{cases} 2.258 \times 10^{-6} \text{ SOC}^{-0.3952}, & T = 293 \text{ K} \\ 1.857 \times 10^{-6} \text{ SOC}^{-0.2787}, & T = 303 \text{ K} \\ 1.659 \times 10^{-6} \text{ SOC}^{-0.1692}, & T = 313 \text{ K} \end{cases}$	[49]
1.25 Ah Sony 18650 cylindrical	$R_e = f(\text{DOD}), 0.8\text{--}1.8$	[52]
20 Ah Lithium-Ion Polymer Battery	$R_{series} = 0.035 + 0.1562 \exp(-24.74 \text{ SOC})$ $R_{trans, s} = 0.04669 + 0.3208 \exp(-29.14 \text{ SOC})$ $R_{trans, l} = 0.04984 + 6.604 \exp(155.2 \text{ SOC})$	[53]
60 Ah prismatic battery	1.61 m Ω (charging) and 0.937 m Ω (discharging)	[54]

Q_{rev} , the second term in Equation (2), characterizes the reversible entropy loss and is a function of the entropy coefficient dE_{oc}/dT , charge density, SOC, and cell temperature and is given by

$$Q_{rev} = -IT \frac{dE_{oc}}{dT} \quad (7)$$

The dE_{oc}/dT can be found from experimental measurements of individual electrodes. For SOC \in [100%, 0%], the stoichiometry ranges are $y \in$ [0.442, 0.936] for the positive electrode ($\text{Li}_y\text{Mn}_2\text{O}_4$) and $x \in$ [0.676, 0.126] for the negative electrode (Li_xC_6). In such a case, the entropic coefficient for the positive electrode [55–57] is expressed by curve-fitting, as shown below (Figure 6a)

$$\frac{dE_{oc}}{dT} = 29.41 \text{ SOC}^6 - 54.18 \text{ SOC}^5 + 20.64 \text{ SOC}^4 + 8.4946 \text{ SOC}^3 - 5.4224 \text{ SOC}^2 + 1.0674 \text{ SOC} - 0.2057 \quad (8)$$

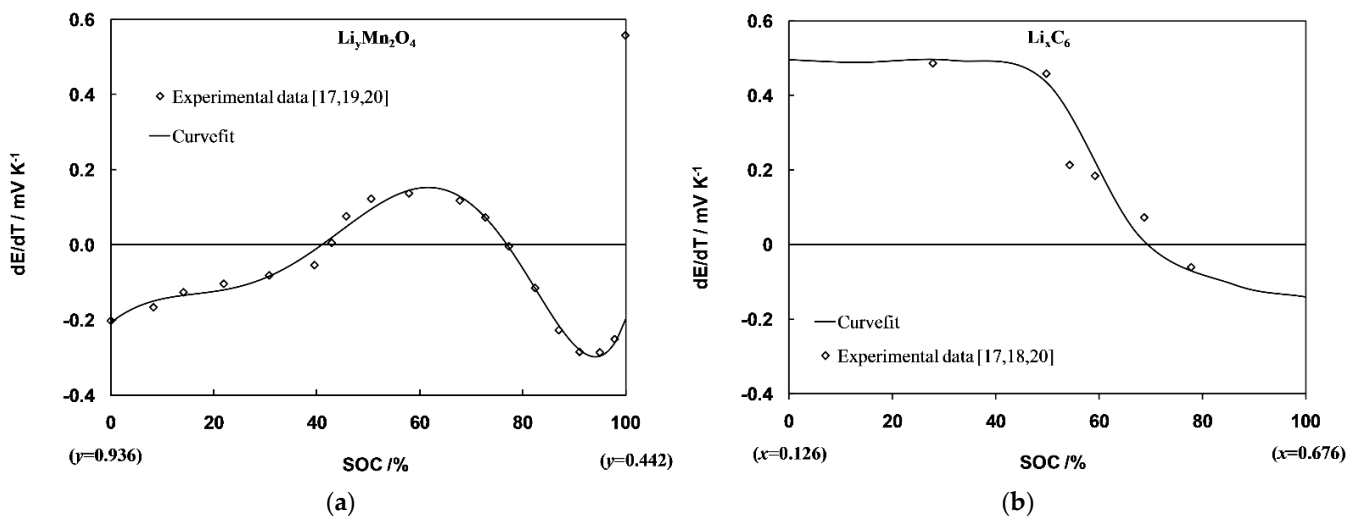


Figure 6. Experimental data of entropic coefficients of the half cells and the corresponding best-fit curves for (a) $\text{Li}_y\text{Mn}_2\text{O}_4$ (positive electrode) [55–57] and (b) Li_xC_6 (negative electrode) [57–59]. Reprinted with permission from [38]. Copyrights 2013 Elsevier.

Similarly, the entropic coefficient for the cathode [57–59] is expressed below (Figure 6b)

$$\frac{dE_{oc}}{dT} = 344.1347148 \frac{\exp(-18.12983079 \text{ SOC} + 4.163332068)}{1 + 749.0756003 \exp(-19.13504805 \text{ SOC} + 4.503478072)} - 0.418400661 \text{ SOC} + 0.109595516 \text{ SOC}^2 + 0.168196519 \quad (9)$$

At high charge and discharge rates, irreversible heat generation is significantly higher than reversible entropic heat generation. Thus, the entropic loss is not always considered for electric/hybrid electric vehicle applications. The Joule heating term varies quadratically with the current. Conversely, the entropic loss increases linearly with current, which may be positive (exothermic) or negative (endothermic) relying on the charging or discharging. Consequently, the net effect of the reversible entropic heat generation could be negligible after a full cycle of charging/discharging.

The convection thermal resistances (R_u in Figure 5) for the cells, NTU for a heat exchanger as a battery pack, Reynolds number, and Nusselt number suggested by Zukauskas and Ulinskas [60–63] for an in-line tube-bank system are expressed as

$$R_u = \frac{1}{(\rho c_p \dot{V})_f (1 - e^{-NTU})} \quad (10)$$

$$NTU = \frac{A_{ku} Nu_{D,p} k_f (1 - \varepsilon)}{(\rho c_p \dot{V})_f D_p \varepsilon} \quad (11)$$

$$Re_{D,max} = \frac{\rho u_{max} D}{\mu} \quad (12)$$

$$Nu_D = \begin{cases} 0.8 Re_{D,max}^{0.4} Pr^{0.36} \left(\frac{Pr}{Pr_w}\right)^{0.25}, & 10^0 < Re_{D,max} < 10^2 \\ 0.51 Re_{D,max}^{0.5} Pr^{0.25} \left(\frac{Pr}{Pr_w}\right)^{0.25}, & 10^2 < Re_{D,max} < 10^3 \\ 0.27 Re_{D,max}^{0.63} Pr^{0.36} \left(\frac{Pr}{Pr_w}\right)^{0.25}, & 10^3 < Re_{D,max} < 2 \times 10^5 \\ 0.021 Re_{D,max}^{0.84} Pr^{0.4} \left(\frac{Pr}{Pr_w}\right)^{0.25}, & 2 \times 10^5 < Re_{D,max} < 2 \times 10^6 \end{cases} \quad (13)$$

The energy conservation equation for the coolant flow over a battery cell is given as

$$Q_{u,i-1} - Q_{u,i} + Q_{ku,i} = 0 \quad (14)$$

$$Q_{u,i-1} - Q_{u,i} = (\rho c_p \dot{V})_f (T_{f,i} - T_{f,i-1}) \quad (15)$$

Here, u_{max} is the maximum flow velocity between the cells. The Nusselt number in Equation (13) is valid only when the number of the cells in the streamwise direction exceeds 20. For the eight-cell system used for this study, a correction factor, $C_2 = 0.95$, is required to correct the Nusselt number in Equation (13), i.e., $C_2 Nu_D$.

2.2. Spatial-Resolution Lumped-Capacitance Thermal Model

It is a common practice to perform the model-based design, both for cylindrical and prismatic cells, using CFD (computational fluid dynamics) approaches, which provide an accurate description of core temperature and time-dependent thermophysical properties and electrical properties. The estimation of core temperature is of much importance, which is sufficiently higher than the surface and average temperature, as estimated by the classical lumped thermal model. However, the CFD modeling has been numerically expensive and computationally not efficient for a fast calculation. In this section, we discuss a spatial resolution lumped thermal model that calculates the core temperature of the cell in a time-efficient manner.

The governing equations based on a cylindrical cell (Figure 7) approximation can be written as

$$\rho_s(T) c_{p,s}(T) \frac{\partial T}{\partial t} = \frac{1}{r} \frac{\partial}{\partial r} \left[r k_s(T) \frac{\partial T}{\partial r} \right] + s(r, t) \text{ for } 0 < r < R \text{ and } t > 0 \quad (16)$$

$$-k_s(T) \frac{\partial T(R, t)}{\partial r} = h_f(t) [T(R, t) - T_\infty(t)] \text{ for } t > 0 \quad (17)$$

$$\frac{\partial T(0, t)}{\partial r} = 0 \text{ for } t > 0 \quad (18)$$

$$T(r, 0) = T_o(r) \text{ for } 0 < r < R \quad (19)$$

where $s(r, t)$ is the volumetric heat generation of a cell.

From an individual cell level consideration, it is rational to assume that the cell is subjected to a uniform temperature and convective heat transfer coefficient at the cell level. Consequently, for a pack with multiple cells, the cell level model can be extended using a flow network model where the ambient temperature will be updated along with the cell as discussed in Section 2.1. In electric vehicles, the coolant air inducts from the cabin air, providing easy access and reliability; although, it has a low convective heat transfer capacity.

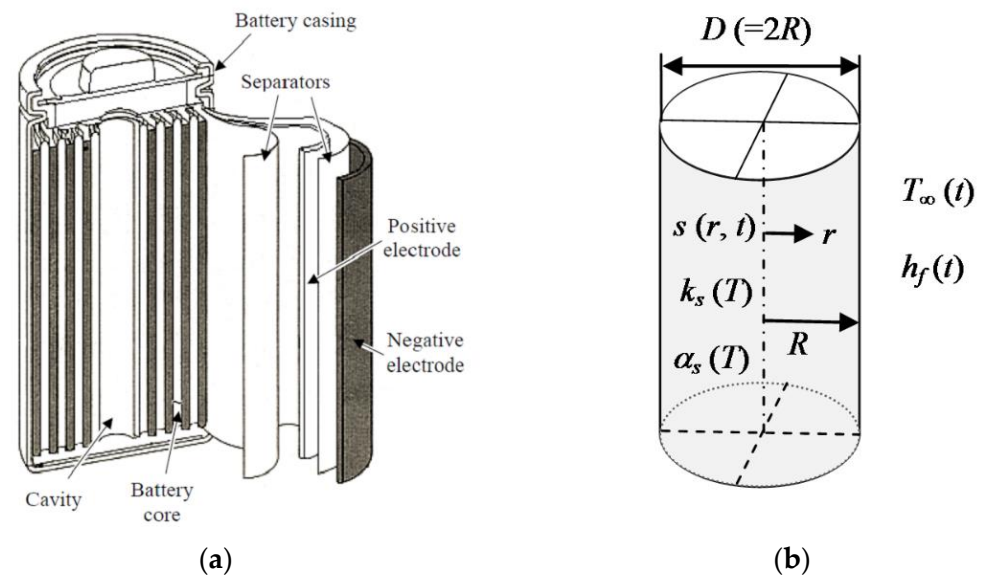


Figure 7. (a) A typical configuration of the spiral and multilayer structure of a standard cylindrical cell [6] and (b) the realistic prediction of cell temperature depends on the actual description of the time-dependent thermal boundary conditions. Reprinted with permission from [38]. Copyright 2013 Elsevier.

The flow network model in Section 2.1 is based on a conventional LC thermal model and assumes a uniform cell temperature that applies to a low Biot number (i.e., $Bi = \frac{h_f R}{k_s} < 0.1$). Conversely, recent advances in high power density and energy density cells require highly efficient cooling mechanisms, such as liquid cooling, where the convective heat transfer coefficient could reach 100 times that of conventional (air cooling). Moreover, larger cells becoming more popular in several applications. Such conditions could result from $Bi > 0.1$ and can result in a larger temperature gradient within the cell with increasing temperature from the surface to the core of the cell. In such cases, the improved lumped thermal model could be applied to correctly estimate battery core temperature [13]. The mathematical formulations of these problems under high Biot number conditions are described in this section [13].

The improved lumped thermal model (spatial resolution LC thermal model) can estimate the core temperature, average cell temperature, and skin (surface) temperature of an individual cell. By definition, the area integrated average cell temperature is called the area-averaged cell temperature. In Figure 7b, it can be written by

$$T_{avg}(t) = \frac{1}{\pi R^2} \int_{r=0}^R (2\pi r) T(r, t) dr \quad (20)$$

Hence, the temporal variation in the $T_{avg}(t)$ (average temperature) can be written as

$$\frac{dT_{avg}(t)}{dt} = \frac{1}{\pi R^2} \int_{r=0}^R (2\pi r) \frac{\partial T(r, t)}{\partial t} dr \quad (21)$$

Equation (16) can be integrated (with respect to r variable) and then combined with the boundary conditions [Equations (16) and (17)] and averaged temperature [Equation (21)] to obtain the following governing equation,

$$\rho_s(T) c_{p,s}(T) \frac{dT_{avg}(t)}{dt} = -\frac{2h_f(t)}{R} [T(R, t) - T_\infty(t)] + s(t) \quad (22)$$

It can be seen that Equation (22) counts both surface and average temperatures [i.e., $T_{avg}(t)$ and $T(R, t)$] in comparison to the formulation of the classical LC model.

The equivalent equation of Equation (22) for the conventional LC thermal model takes that the temperature gradient is significantly small when $Bi < 0.1$, i.e., $T(R, t) = T_{avg}(t)$. Hence Equation (22) for the conventional LC thermal model takes the following form

$$\rho_s(T)c_{p,s}(T)\frac{dT_{avg}(t)}{dt} = -\frac{2h_f(t)}{R}[T_{avg}(t) - T_\infty(t)] + s(t) \quad (23)$$

On the contrary, for a high Biot number (i.e., $Bi > 0.1$), the temperature gradient in the radial direction would be significantly high that a correlation between the surface and the average temperature is necessary [64]

$$T(R, t) \cong f[T_{avg}(t)] \quad (24)$$

The aforementioned correlation of skin (surface) and average temperatures was formulated from the Hermite-type integral approximation. Where the accuracy depends on the number of terms used for the analytical derivation. The analytical derivation and accuracies of the Hermite approximation are expressed as $H_{i,i}/H_{j,j}$, where the indices i , and j represent the degree of the Hermit integration. In addition, the first part corresponds to the accuracy in average temperature, $T_{avg}(t)$ and the second part corresponds to the accuracy of the temperature gradient $\partial T(r, t)/\partial r$.

For instance, the Hermite approximation based on $H_{0,0}/H_{0,0}$ is formulated on the zero-order ($H_{0,0}$) formula, corresponding to the classical trapezoidal formulation for the average temperature and temperature gradient as expressed below

$$T_{avg}(t) \cong \left[\frac{1}{2}T(0, t) + \frac{1}{2}T(R, t) \right] \quad (25)$$

$$T(R, t) - T(0, t) \cong \frac{R}{2} \left[\frac{\partial T(0, t)}{\partial r} + \frac{\partial T(R, t)}{\partial r} \right] \quad (26)$$

Solving the Equations (25) and (26) for the surface temperature and applying the boundary conditions, Equations (17) and (18),

$$T(R, t) = \left[1 + \frac{Bi}{4} \right]^{-1} [T_{avg}(t) - T_\infty(t)] + T_\infty(t), \quad Bi = \frac{h_f R}{k_s} \quad (27)$$

The average temperature $T_{avg}(t)$ is obtained by solving the energy Equation (22) with the following initial condition

$$T_{avg}(0) = T_o \quad (28)$$

The skin (surface) temperature $T(R, t)$ and core temperature $T(0, t)$ can be calculated from Equations (25) and (26).

Correspondingly, $H_{1,1}/H_{0,0}$ represents the first-order formulation ($H_{1,1}$) for temperature and the zeroth-order formulation ($H_{0,0}$) for temperature gradient. The zeroth-order Hermite approximation represents the conventional trapezoidal formula, whereas the first-order formula could be written by the corrected trapezoidal formula. Based on the $H_{1,1}/H_{0,0}$ formulation, the average temperature can be written by

$$T_{avg}(t) \cong \left[\frac{1}{6}T(0, t) + \frac{5}{6}T(R, t) \right] + \frac{Bi}{6}[T(R, t) - T_\infty(t)] \quad (29)$$

The models were tested for a stepwise discharge current profile representing periodic charging and discharging and for a real battery load cycle under the Federal Urban Duty Cycle (FUDS). A significant deviation in average cell temperature prediction is observed in Figure 8a based on the lumped thermal model and the Hermite integration approach ($H_{0,0}/H_{1,1}$, and $H_{1,1}/H_{1,1}$) for a $Bi = 5$ case study. Figure 8a also shows the improved lumped thermal model based on the Hermite integral approximation could closely match

the exact solution based on Green’s function method [38], except for the classical lumped thermal model. Figure 8b compares the core, average, and surface temperatures based on the Hermite approximation; a good match with the exact solution was found for all these temperatures. Based on a simple step-wise profile both the $H_{0,0}/H_{1,1}$, and $H_{1,1}/H_{1,1}$ Hermite approximations accurately estimates these temperatures. As the model is validated by the exact solution the model was further tested for the actual battery duty cycle based on the FUDS, as shown in Figure 9a,b. As illustrated in Figure 9a, the model was tested for the average cell temperature under three Biot number conditions under a FUDS cycle. Deviation of core, skin, and averaged temperatures were also found for high Biot number conditions for a FUDS cycle, suggesting that an improved lumped thermal model would be essential to correctly estimate the average cell temperature and thermal management performance under a FUDS cycle.

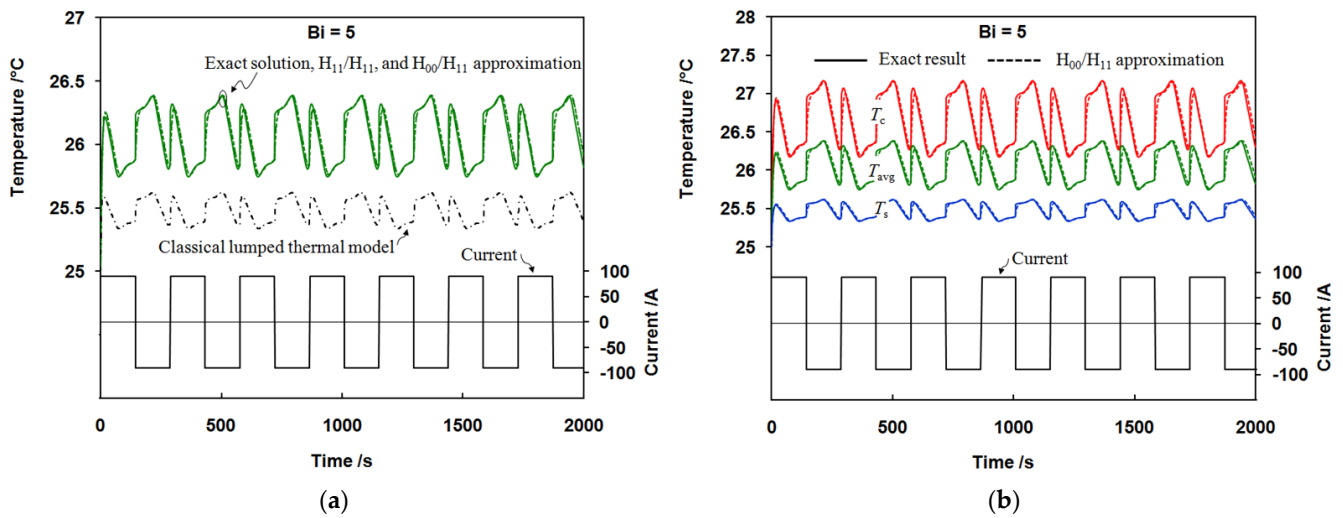


Figure 8. Application and validation of improved LC thermal model: (a) The average temperatures (T_{avg}) from the analytical result and the improved LC model for a stepwise duty cycle and $Bi = 5$. (b) Prediction of core, skin (surface), and average temperatures for this cycle. Reprinted with permission from [38]. Copyright 2013 Elsevier.

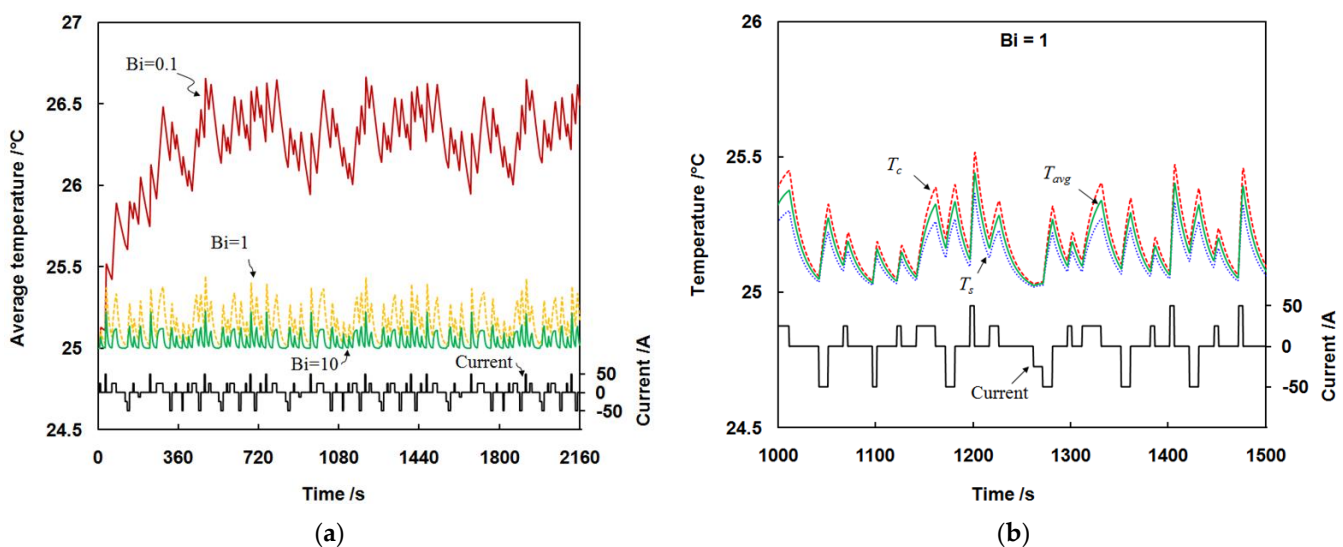


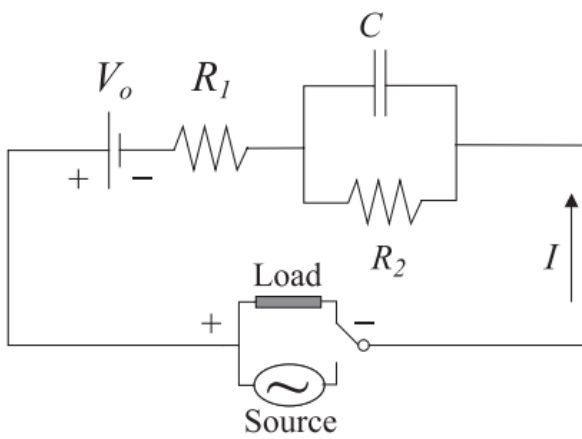
Figure 9. (a) The prediction of average cell temperature under three Biot numbers and (b) core, surface, and average temperatures for $Bi = 1$ based on $H_{0,0}/H_{1,1}$ approximation under a FUDS cycle. Reprinted with permission from [38]. Copyright 2013 Elsevier.

2.3. Equivalent-Circuit Model (ECM)

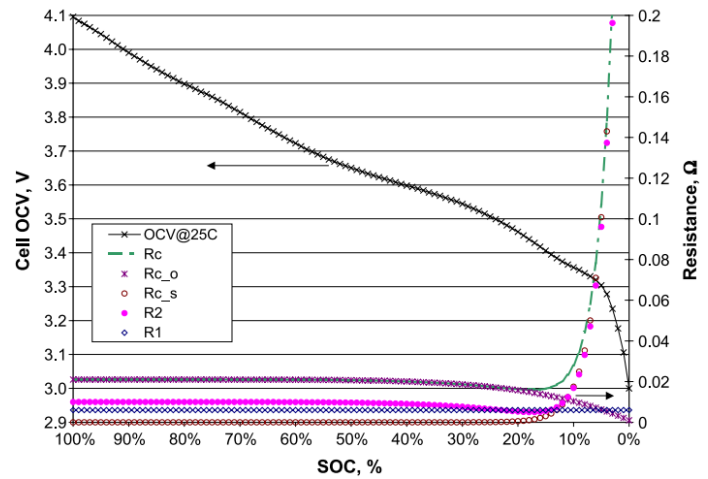
In the ECM approach, the associated equivalent circuit can be used as a tool to predict battery behavior [40–42]. As shown in Figure 10, according to Liaw et al. [40], an ECM may comprise three major parts: a static part representing the thermodynamic properties according to cell chemistry, such as the nominal capacity and open-circuit voltage (OCV) in terms of SOC. Secondly, a dynamic part represents the kinetic aspects of the cell’s internal impedance behavior. Finally, a source or load to complete the circuit for a charge or discharge regime allows mimicking the battery behavior and simulating its performance characteristics. To apply ECM, SOC-dependent OCV and resistance values are required from experimental measurement. Afterward, the cell voltage can be simulated under the constant current assumption, as described by [65]

$$V(t) = \frac{S(0)}{C} e^{-\frac{t}{R_2 C}} + V_o - IR_1 - IR_2 \left(1 - e^{-\frac{t}{R_2 C}}\right) \tag{30}$$

where $S(0)$ is the capacity, and V_o is the nominal SOC-dependent cell OCV. Equation (30) can be used to calculate the cell voltage change at various rates. Therefore, a simulated voltage versus SOC (or time) discharge curve for a specific rate can be obtained.



(a)



(b)

Figure 10. (a) The equivalent circuit model of Liaw et al. [40–42], to simulate LiB performance for Gen 2 cells (b) The SOC-dependent OCV and resistance values for the total cell resistance (R_c and the two independent contributions R_{c_o} and R_{c_s}), R_1 , and R_2 of the Gen 2 chemistry in the model. Adapted with permission from [40]. Copyright 2014 Elsevier.

A thermal equivalent circuit model (TECM) was also proposed by Gan et al. [42] where thermal resistance, heat capacities, and heat generation rates of each component within the BTMS were connected. The temperature response of each component was calculated based on the energy balance [17]

$$C \frac{dT}{d\tau} = S_{int} + S_{in} - S_{out} \tag{31}$$

where C is the heat capacity, S_{int} is the internal heat generation, S_{in} is the heat flow into the component, and S_{out} is the heat flow out the component.

$$S_{in} \text{ or } S_{out} = \frac{\Delta T}{R_t} \tag{32}$$

where ΔT is the temperature differential among two nodes in the TECM, and R_t is the thermal resistance.

The temperature responses of several key measuring points in the BTMS are used in the comprehensive experimental validation with discharge rates, flow rates, and inlet temperatures.

Similarly, an electro-thermal model was discussed by Lin et al. [66] comprising an electrical model and a two temperatures model. These two parts were coupled through SOC, current I , and electrical parameters. The coupled electro-thermal model was able to capture the core cell temperature as validated by the experiment.

In the model, the terminal voltage V_T is modeled as follows,

$$V_T = V_{OCV} - IR_s - \sum_{i=1}^n V_{RC,i} \quad (33)$$

In Equation (34), V_{OCV} refers to open-circuit voltage and depends on SOC, I is the discharge current, and R_s is the ohmic resistance. IR_s refers to a voltage drop across the resistor and V_{RC} refers to a voltage drop across a parallel RC circuit.

The \sum term refers to a series of parallel RC circuits. The transient voltage profile of an individual RC element can be formulated by

$$\frac{dV_{RC,i}}{dt} = -\frac{1}{R_i C_i} V_{RC,i} + \frac{1}{C_i} I \quad (34)$$

The model solved for two temperatures (core and surface) from two governing equations by assuming a longitudinal homogeneity as below

$$C_C \frac{dT_c}{d\tau} = S_{irr} + \frac{T_s - T_c}{R_c} \quad (35)$$

$$C_s \frac{dT_s}{d\tau} = \frac{T_f - T_s}{R_u} - \frac{T_s - T_c}{R_c} \quad (36)$$

where C_C is the heat capacity of the cell materials, C_s is the heat capacity of the can, and S_{irr} in Equation (36) can be evaluated as follows

$$S_{irr} = I(V_{OCV} - V_T) \quad (37)$$

As shown in Figure 11a, the communication between the electrical and the thermal model occurs via heat generation and temperature-dependent properties. In the electrical model, the discharge voltage [Equation (34)] and SOC were solved based on temperature-dependent parameters R_s , R_i , and C_i . Subsequently, the cell heat generation was estimated using the formulation $I(V_T - V_{OCV})$, before using the thermal model to estimate the core temperature, T_c , and the surface temperature, T_s , of the cell. The core temperature in this model denotes the lumped electrode temperature, which can be used to estimate R_s , R_i , and C_i .

The voltage, as well as temperatures predicted with the model, are shown in Figure 11b. The major advantages of this approach were the two-temperature model and the estimation of the core or lumped electrode temperature. This provides an added benefit in precisely estimating temperature-dependent R_s , R_i , and C_i of the electrical model and subsequently calculating the discharge voltage. This method could be significantly beneficial under two scenarios, where a large temperature gradient is present within the cell volume, such as a high Biot number condition and high current application. A combined battery thermal management system of such a coupled electro-thermal model is depicted in Figure 12 [67,68].

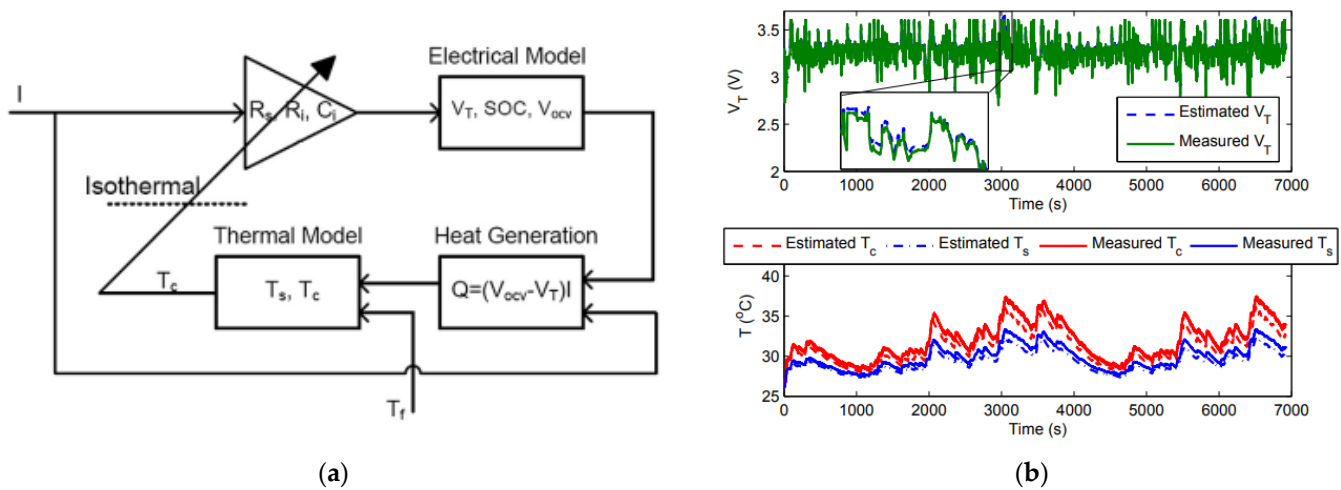


Figure 11. (a) A schematic representation of the electrical and thermal models. (b) Voltage and temperature estimation under the charge-sustaining cycle. Reprinted with permission from [66]. Copyright 2014 Elsevier.

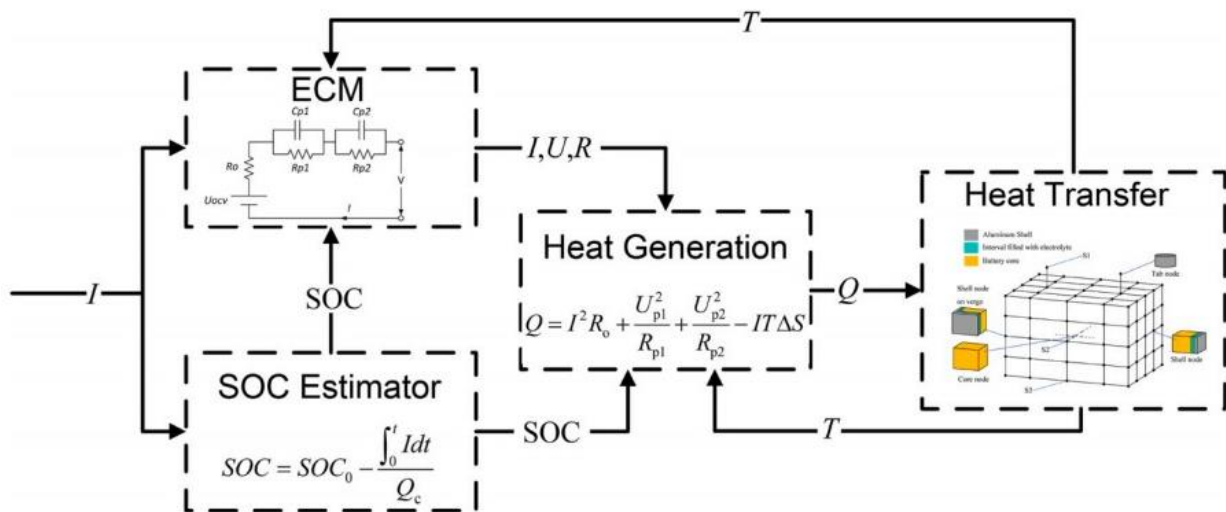


Figure 12. Schematic illustration of the multi-node and coupled electro-thermal concept. Reprinted with permission from [67]. Copyright 2020 Elsevier.

2.4. Impedance-Based Temperature Detection (ITD) Model

As proposed by Richardson et al. [43,44], impedance-based temperature detection is an efficient method (as impedance can correlate with volume-average temperature) of temperature estimation, whereby the internal cell temperature is directly inferred from online electrochemical impedance spectroscopy (EIS) measurements at a single frequency (Figure 13). These methods have unique advantages and disadvantages. The ITD/T method is independent of the battery thermal properties, heat generation, and boundary conditions. Instead, it requires both a thermocouple and impedance measurement on each cell and so its instrumentation cost may be prohibitive. Moreover, although it overcomes the requirement for a thermal model, it still relies on a Pseudo-Steady-State temperature approximation. However, it requires only a single measurement input—the impedance metric—and thus has the potential to substantially reduce instrumentation costs in real-time measurements.

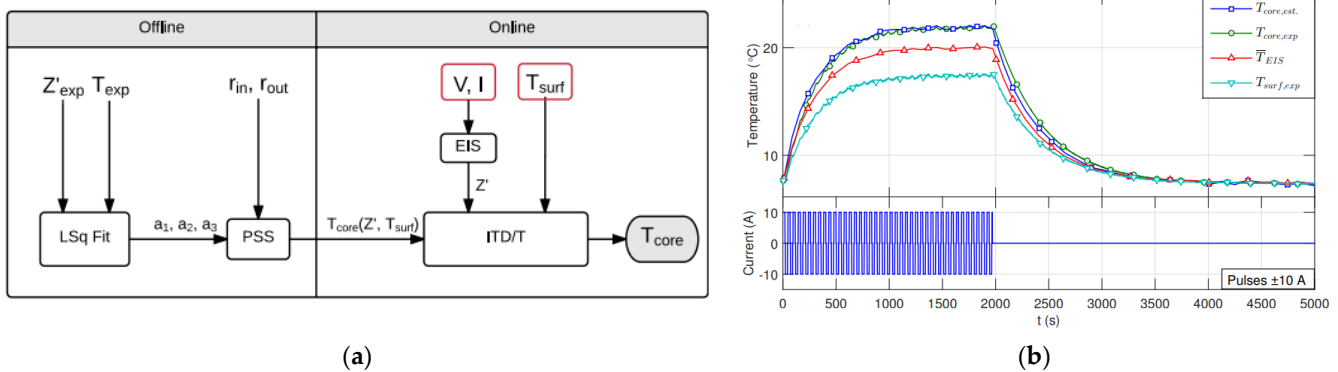


Figure 13. (a) A description of the Hybrid method of temperature estimation in an impedance-based model. Reprinted with permission from [44]. Copyright 2016 Elsevier. (b) Model estimates and current pulse experimental results: ± 10 A [42,43,68]. Reprinted with permission from [69]. Copyright 2014 Elsevier.

2.5. Data-Driven Model and Implementation of IoT-Cloud Infrastructure

The numerical modeling of BTMS requires many nonlinear equations comprising the Navier stokes equation and species conservation equations, requiring a rigorous computational effort. Hence, data-driven modeling could be an efficient alternative method considering that prior knowledge and available data to train the algorithm are available. Due to increasing demand, different algorithms of data-driven methods have been applied in EVs, including machine learning [45,70,71], Gaussian process optimization [72,73], artificial neural network [46,74,75], and foster network [76]. Other advantages are that such systems can feedback cell and pack level information, thus providing the benefits of a comprehensive multiphysics model [75,77]. Though data-driven modeling can be reliable, it requires an infinite amount of data, data storage, and computational power. Hence, the cyber-physical modeling integrated with IoT and cloud infrastructure could probably eliminate these limitations and can provide resource optimization or necessity of long time-algorithm training process providing the fact that intelligent sensors and control along with essential infrastructure are available. Such a system is shown in Figure 14. IoT cloud-enabled systems have already been proposed for several applications in EVs including autonomous driving [78–80], wireless charging [81], battery management [82], and connected vehicles [83].

In Section 2, four different LC models were discussed to evaluate average cell temperature or core and surface temperatures based on different algorithms and coupling of heat generation. The relative advantages and disadvantages of the LC models, numerical models, and the equivalent circuit model were discussed in [84]. The accuracy of these methods varies with the level of discretization, algorithm, and measurement data, and therefore it would be quite impossible to precisely quantify the level of accuracy among those methods. However, it can be optimally said that depending on the application, different methods can be applied. In terms of the number of equations and level of complexity, a relative computational time and effort comparison of the five different approaches is depicted in Figure 15, though these comparisons are not completely objective and can vary depending on applications.

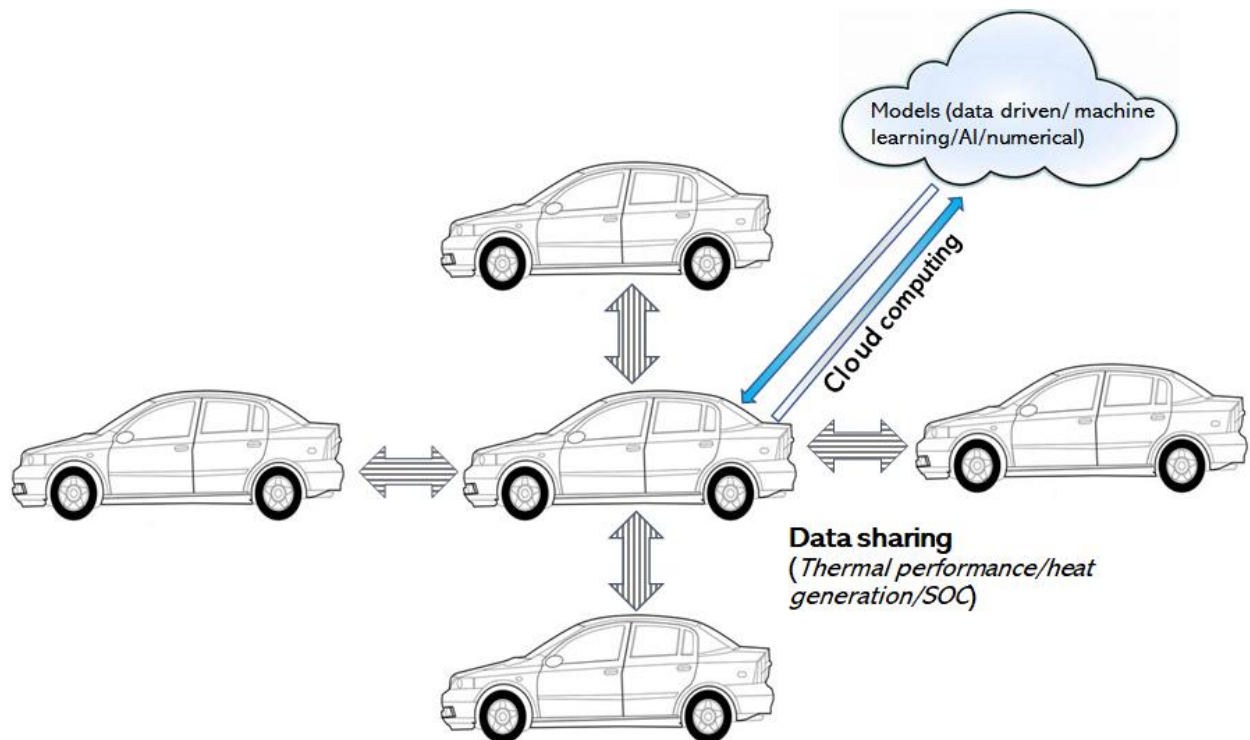


Figure 14. Schematic representation of a proposed IoT-cloud enabled structure that particularly could benefit big data and data-driven modeling-based BTMS approach for fast training, thermal performance optimization, and minimization of in-house computational efforts.

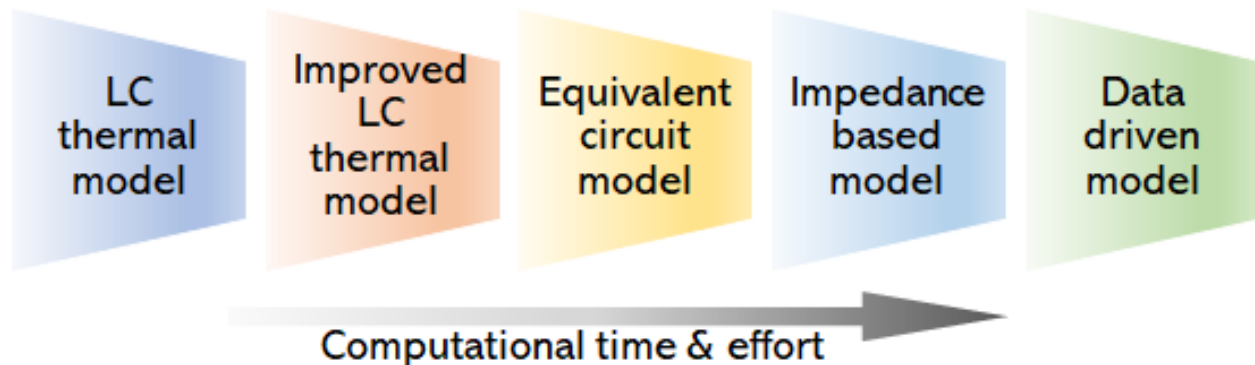


Figure 15. Assessments of computational time and effort of the five modeling approaches.

3. Thermal Management Practices

3.1. Air-Driven Battery Thermal Management

The air-based BTMS is most popular as it is most convenient and easy-to-implement in the conventional framework. The effectiveness of such a system relies on two factors, the effective heat transport process and the minimization of the thermal boundary layer. In addition, there are many other variables such as inlet temperature, pressure, ambient conditions, and spacing, which are vital for the effective design of air-based BTMS. The air-based BTMS can be of many types and are described in the following subsections.

Conventional air-cooling: The conventional air-cooling system has mostly been studied by experiments and modeling, where either the natural or cabin air is passed across the battery pack to decrease the cell temperature and optimize the battery performance (Figures 16 and 17). Air-based thermal management techniques are the most common practice and are covered extensively in the literature for several configurations. The effects of serial and parallel ventilation on the cooling performance were studied by Pesaran

et al. [85]. Parallel ventilation cooling was found to be highly effective as it can decrease the cell temperature (maximum) by 4 °C and the pack temperature differential by 10 °C in comparison with serial ventilation cooling. This may be because parallel ventilation provides an effective means of boundary layer destruction. The correlation between the thermal performance and the cell arrangement was numerically studied by Wang et al. [86]. According to the study, the air cooling performed better with the axisymmetric battery structure because of the minimization of the boundary layer (thermal) structure. The authors also recommended that better performance could be achieved by positioning the fan on the roof of the module. The influence of the cell spacing on the cell temperature was studied by Yang et al. [87,88] suggesting that the maximum battery cell temperature rises in proportion with the spacing between cells. Afzal et al. [89,90] also came to a parallel conclusion, where a drop in maximum cell temperature with a reduction in spacing was attributed to increased fluid mean velocity.

Comparably, Park et al. [91] applied liquid and air-based BTMS on different cell arrangements to enhance the thermal performance and optimum operating conditions. Similarly, Sun et al. [92] improvised a Z-type air flow by utilizing a tapered inlet/outlet and improved the performance of the parallel air-based BTMS. When tested with the US06 drive cycle, this improvised design decreases the cell temperature (maximum) by 8.0 °C and the temperature differential by 1.1 °C in comparison to the baseline Z-type flow settings. This improved design could also enhance the pressure drop performance. For example, the pressure drop was reduced by 43% (at $0.0283 \text{ m}^3 \text{ s}^{-1}$) compared to the baseline condition. Chen et al. [93] performed structural optimization of a parallel air-based design that could decrease the temperature differential by a maximum of 45%. The proposed method employs a unique approach to improve the flow performance by maintaining a uniform flow in all the channels by optimizing the plenum width and retaining the same battery configuration. This type of structured optimization was found to be efficient and could reduce the cell temperature and the pack temperature differential by 0.2 K and 2.3 K, respectively, compared to the baseline condition.

Jiaqiang et al. [94] performed a CFD simulation and evaluated the cooling performance depending on the arrangement of the inlet and outlet duct. Placing the inlet and outlet on opposite walls was found to be more efficient than placing them on the same side. As this enhances the mechanism of mixing and boundary layer destruction, positioning the inlet/outlet ducts on the counter side can improve the temperature uniformity in the battery pack. They also achieved a higher thermal performance by using baffle plates in the flow channel, which enhanced flow mixing. Shahid et al. [95] introduced an inlet plenum to achieve a higher thermal performance in a pack containing 32 cells. Based on this configuration, the cell temperature and temperature nonuniformity could shrink by the order of 18.3% and 54.6%, respectively. However, the proposed inlet plenum did not significantly enhance the performance above the critical Reynolds number (7440). Hong et al. [96] applied an additional outlet in air-based BTMS and decreased the maximum cell temperature by a minimum of 5 K. The application of a second vent also reduced the temperature differential by 60% as compared with a system with no vent. Additionally, the thermal performance could be further enhanced by increasing the width of the secondary vent.

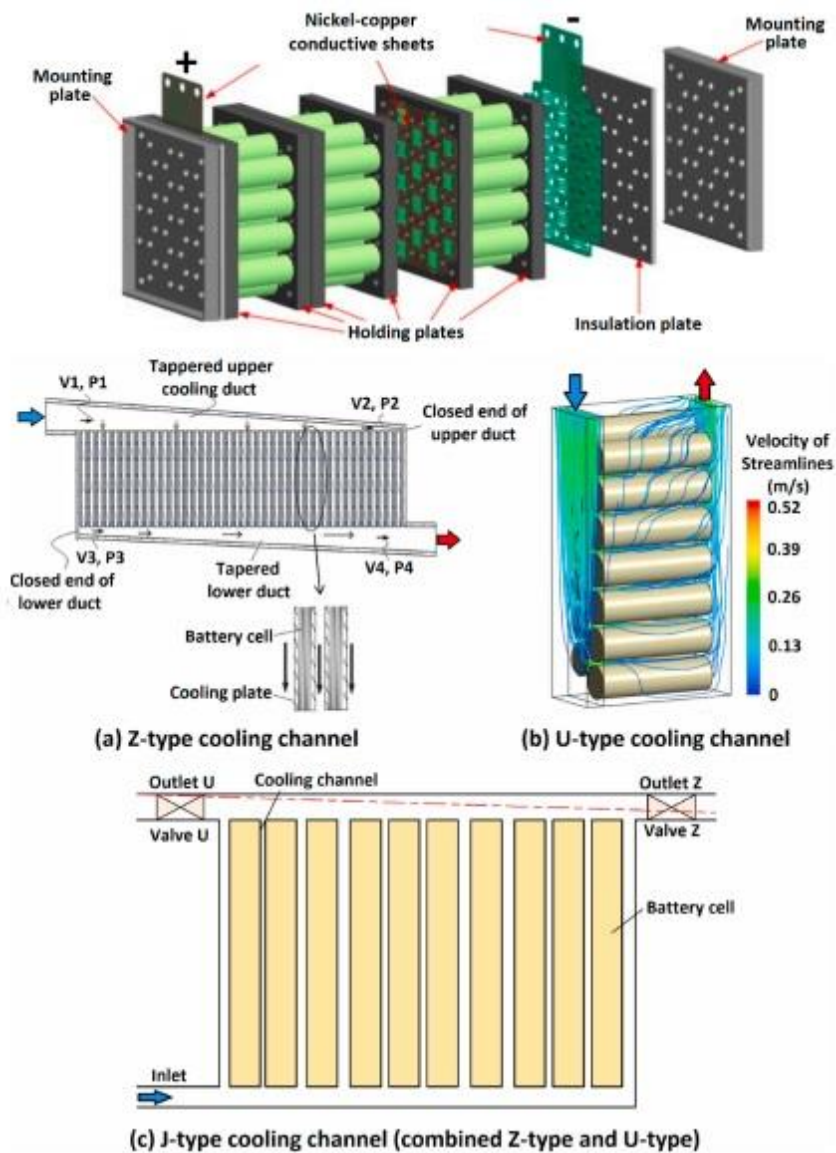


Figure 16. Air-based thermal management, as one of the most convenient forms of techniques, can be optimized using a different configuration of the cooling channel [(a) Z, (b) U, or (c) J type] [16,97]. Reprinted with permission from [97]. Copyright 2021 Elsevier.

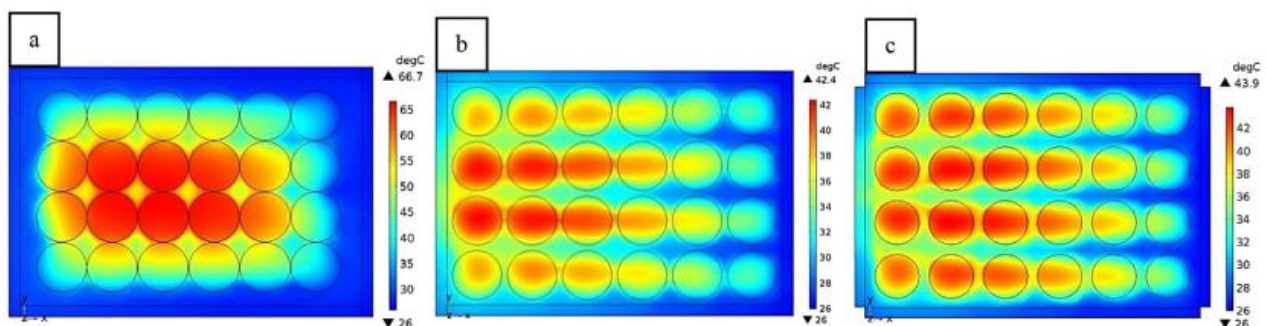


Figure 17. Simulation of temperature distribution in an air-cooled system for different cell spacings at a discharge rate of 1.5 C for an inlet flow of 2 m/s, and an initial temperature of 26 °C [98]. Cell spacings for the simulation: (a) 0, (b) 2, and (c) 4 mm. Reprinted with permission from [98]. Copyright 2020 Elsevier.

Yi et al. [99] devised a mathematical model to investigate the role of aging on the electro-thermal behavior of a Li-ion cell for the applications of EVs and PHEVs. In addition, they studied the thermal performance of the pack based on operating conditions. Choe et al. [100] showed that the cell temperature was increased as the inlet air temperature increased; however, the temperature differential in the pack reduced as the heat generation rate decreased. In a study by Fan et al. [101], escalating the inlet flow rate improved the thermal performance achieved in the pack. These results were expected because the increase in the air flow velocity improved the convective heat transfer coefficient. However, there is an up to certain maximum inlet airflow rate where the cooling performance increases as suggested by Liu et al. [102]. For example, He et al. [103] observed that the growth of the flow rate diminishes the field synergy number and decreases the efficiency of air utilization. Table 3 represents some of the recent development in air-based BTMS.

Table 3. Recent developments in air-based battery thermal management methods.

Authors	Strategies	Recommendations	Methods
Park et al. (2013) [91]	Air flow configuration	Numerical modeling was performed with different cell arrangements. It is recommended that the design and fluid of BTMS should depend on the heating load. In addition, smaller cell spacings were recommended for air-based BTMS.	Numerical simulation
Xu et al. (2013) [104]	Air flow configuration	The heat transfer performance was enhanced by converting a longitudinal array into a horizontal battery array.	Numerical simulation
Wang et al. (2014) [86]	Arrangement of cells and inlet/outlet	A BTMS was studied with different cell arrangements in the pack, cell spacing, and fan location (air cooling). The authors proposed a fan on the top, a cubic cell arrangement, and a hexagonal structure of the cells in the pack for optimum module performance.	Numerical simulation
Sun et al. (2014) [92]	Geometries of inlet and outlet flow ducts	Two supplementary outlet vents were placed directly opposite the main outlet to increase the flow uniformity in the flow conduits. The modified design decreased the temperature differential by 1.1 °C and the cell temperature (maximum) by 8.0 °C compared to the base case.	Analytical, numerical simulation
Yang et al. (2015) [87]	Effects of longitudinal and transverse spacing	The significance of longitudinal and transverse spacing was studied for the thermal performance based on aligned and staggered arrays. The cell temperature increased for either aligned or staggered arrays if the transverse spacing was increased. The cell temperature (maximum) increases proportionally with the increase in the longitudinal spacing for staggered configurations and inversely proportional for aligned arrays.	Experiment, numerical simulation
Wang et al. (2015) [105]	Impact of ambient temperatures, discharge rates, and cooling conditions	The optimum operating air temperature range was proposed as 20–35 °C. However, when the air temperature is within 35–40 °C, an increment of flow velocity by 1 m/s was suggested. However, no forced convection cooling was indicated when the ambient temperature dropped below 20 °C.	Numerical simulation

Table 3. Cont.

Authors	Strategies	Recommendations	Methods
Saw et al. (2015) [106]	Effects of various mass flow rates to predict a correlation between the Nu and Re	A new method of improving the thermal performance was proposed based on numerically derived Nu vs. Re correlation by conducting steady simulations at different flow rates and studying them for different charging conditions. The proposed method provides an efficient solution for large-scale systems.	Numerical simulation
Erb et al. (2017) [107]	Optimization of the cell size to minimize the cost of the blower	An analytical method was applied to optimize the cell size in a pack. The optimum cell size can enhance thermal performance and reduce pressure drops. The authors also indicated that the blower cost could be doubled or tripled if the cell was not optimized (cell-wise, either larger or smaller).	Analytical
Shahid et al. (2018) [95,108]	Improvement of mixing and turbulence	Passive cooling (based on forced air) was used to generate mixing and turbulence in the coolant and increase the temperature homogeneity in the pack. The proposed design reduced the cell temperature (maximum) by ~4% and enhance the temperature homogeneity by ~39%.	Numerical simulation
Jiaqiang et al. (2018) [94]	Baffles and different arrangements of inlet/outlet	Placing the inlet and outlet on opposite edges was found to be more efficient than if they were placed on the same side. The authors also achieved a higher thermal performance by using baffle plates in the flow channel, which enhanced flow mixing.	Numerical simulation
Na et al. (2018) [109]	Multi-layered flow channel by the partitions (reversed layer flow).	A method of reversed layer flow was proposed to enhance the temperature homogeneity. The proposed method could reduce the temperature differential by 1.1 °C compared to the unidirectional flow. Further improvement was achieved by adding rectifier grids during air ingress; this initiated turbulence mixing at the entrance, reducing the maximum temperature by ~0.5 °C and the temperature differential by ~0.6 °C (54.5% reduction).	Experiment, numerical simulation
Hong et al. (2018) [96]	Application of a secondary vent	An optimally designed and placed secondary vent could significantly enhance the thermal performance of the pack. Applying this method decreased the maximum cell temperature by at least 5 K and the pack temperature differential by at least 60%.	Mathematical analyses
Chen et al. (2019) [110]	Optimization of cell spacing	Compared to the typical BTMS, the maximum temperature for the optimized BTMS was reduced by ~4 K, whereas the pack temperature differential could be decreased by at least 69% even when the flow rate is different.	Numerical simulation

Table 3. Cont.

Authors	Strategies	Recommendations	Methods
Fan et al. (2019) [101]	Arrangement of cells (aligned, staggered, and crosses)	The aligned arrangement had the best cooling performance and temperature homogeneity, followed by the staggered and lastly the cross arrangement; however, the aligned arrangement had the lowest power consumption, up to 23% less than that of the cross arrangement.	Numerical simulation
Peng et al. (2019) [111]	Thermal inconsistency, inlet/outlet configurations, and cell spacing	An alternative approach to inlet and outlet vent arrangement (both on the same side) was proposed. The authors recommended that the height of the inlet duct played a significant role in the cell temperature and pack temperature differential reduction, reducing sensitivity to the height of the outlet vent.	Numerical simulation
Liu et al. (2019) [102]	J-type air-based thermal management system is proposed and optimized	The authors suggested that a Z-type cooling flow that could switch between U and Z-types could significantly enhance the cooling performance. The proposed J-type was found to be more efficient than the U and Z-types and could provide a ~32% reduction in the temperature rise.	Numerical simulation, experiment

Reciprocating-air cooling: A reciprocating flow designed by a recurrent change in the flow direction was applied [36] and optimized to improve the thermal performance of the pack by periodic destruction of the thermal boundary layer. A design advantage of the reciprocating flow is that it can maintain the battery and use a single blower while adding an external channel with a flip door valve assembly that can be easily controlled and periodically changed, as shown in Figure 18. The design could be further simplified by using a reversible blower that can periodically alter the flow direction to the same setting as a unidirectional flow system. The alternate flow reversal provides a twofold advantage. Firstly, it can destroy the boundary layer at the outlet by reversing the flow; thus, only cells at the center have significant boundary layer development, which is still lower than for the unidirectional flow. These can reduce the maximum cell temperature and temperature differential by heat redistribution. Secondly, by hindering the boundary layer development, the pressure drop could also be reduced across the duct. The modeling results suggested that the thermal performance increases and the cell temperature (maximum) and pack temperature differential are reduced as the reciprocating period is decreased. Based on mathematical and numerical modeling, for a reciprocating period of $\tau = 120$ s, the cell temperature (maximum) was diminished by 4 °C and the pack temperature differential by 1.5 °C in contrast to the baseline flow condition (Figure 19). An experimental study for a standard setup predicted that such flow configuration decreased the temperature nonuniformity by a maximum of 4 °C and reduce the cooling flow by 38% [112].

Air-based systems are the most common and cost-effective practice for thermal management in a majority of applications. The system can use cabin air from the air conditioning unit, thus sometimes eliminating the requirements of any additional cooling unit. The system also operates better in cold temperatures, where a heating unit can be easily installed or heated air from the cabin can be utilized. Major drawbacks of air-based systems are a relatively lower heat transfer coefficient and temperature nonuniformity in the pack resulting in abruptly high temperature in parts of the pack where the flow is blocked. However, as discussed by applying reciprocating air flow or optimum modeling of the flow channel configuration, these drawbacks can be minimized.

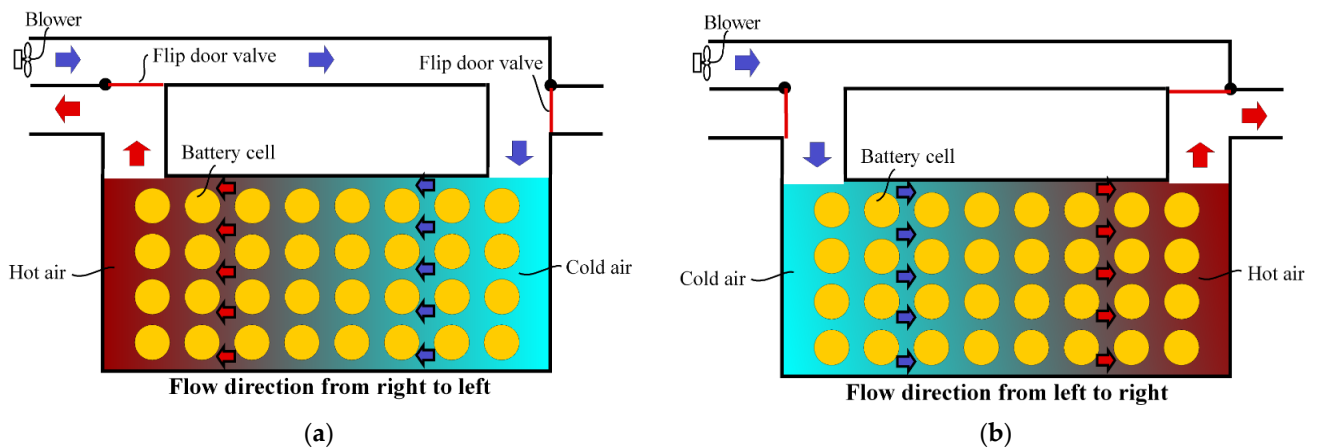


Figure 18. The setup of reciprocating cooling flow configuration in a 2-D schematic view is presented for a pack with 4 by 8 cells. Flow directions are altered periodically as (a) first half cycle (right to left) and (b) second half cycle (left to right). Reprinted with permission from [35]. Copyright 2011 Elsevier.

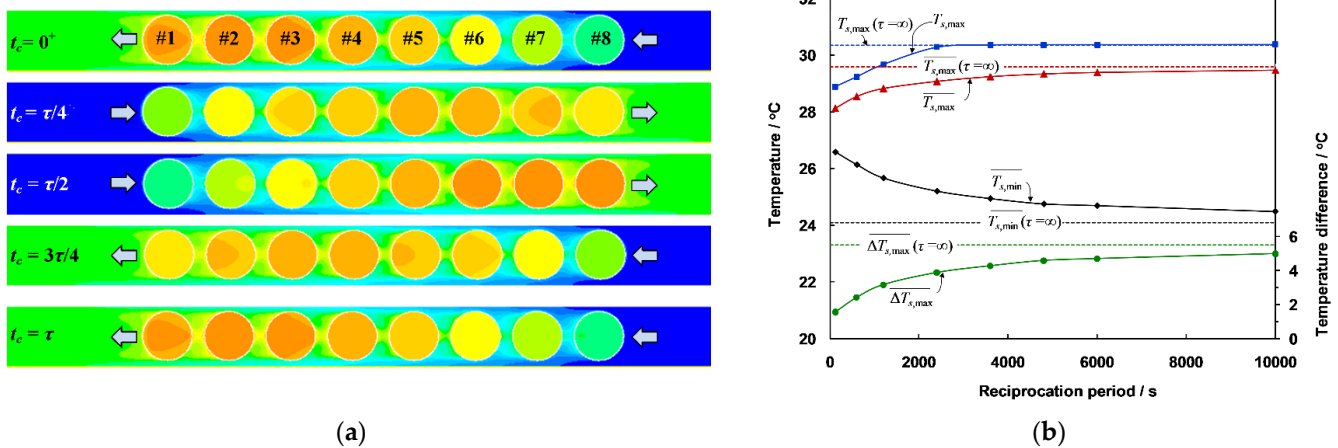


Figure 19. (a) Spatio-temporal profile of temperature contour over a full cycle. (b) The effect of the reciprocating period on the maximum cell temperature and the pack temperature differential. Reprinted with permission from [35]. Copyright 2011 Elsevier.

3.2. Liquid-Based Thermal Management

Liquid cooling allows better thermal control than conventional air cooling when all other heat exchanger parameters are the same. The most common liquid coolant used for a BTMS is a water/ethylene-glycol 50%/50% mixture. The liquid coolant is also volumetrically efficient (HX sizing) as the heat capacity of liquids is significantly greater than that in the air [113]. These added benefits involve increased weight and complexity in manufacturing and design. Therefore, they are only applied when these complexities optimize the thermal performance. They are typically applied with large EVs and PHEVs, such as the Ford Focus or Chevrolet Volt. The liquid-based BTMS can involve direct contact cooling and passive (indirect) contact cooling (Figure 20). Table 4 summarizes some of the recent development in liquid based BTMS.

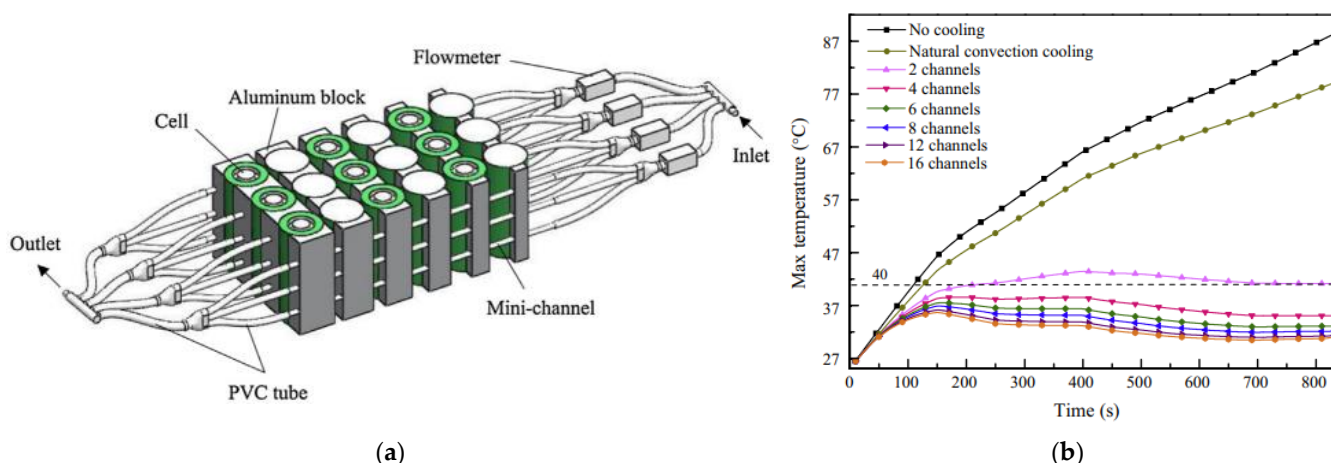


Figure 20. (a) Schematic representation of mini channel liquid cooling. Reprinted with permission from [114]. Copyright 2018 Elsevier. (b) The effect of number of mini-channel cooling channels on the maximum cell temperature (5C discharge). Reprinted with permission from [115]. Copyright 2015 Elsevier.

Direct liquid cooling: In direct liquid cooling, the heat transfer process is controlled by conduction and convection by the surface of the battery. The heat transfer fluid should have higher thermal conductivity, lower viscosity, and lower density; whereas it should have lower corrosion properties and reaction capability with the battery material. The major fluids, such as water and oils (e.g., mineral, silicon,) can be employed for BTMS applications. In addition, boiling liquids and nanofluids have also been involved in the battery thermal management application as they can support a significant improvement in the thermal transport and heat transfer coefficient. It is also a common practice to mix ethylene glycol with water during the winter season to prevent any freezing or so as mentioned. Generally, oil-based coolant provides a better heat transfer coefficient, while its high viscosity significantly increases the pressure drop, consequently increasing the pumping power.

Mineral oil-based coolants have also been tested and found to be performed better than the water-based system at the cost of higher weight. A comprehensive computational study of the different spacing and coolant types was studied by Park and Jung [91]. The study suggested that air cooling provides better performance for a larger cell with smaller inter cell-spacing, whereas the liquid-based system can perform better for a narrow cell design. A comprehensive experiment of water-based cooling showed that liquid-based BTMS was 3000 times more effective than the air-based BTMS, whereas the parasitic loss was reduced by 40% [116].

Boiling and nanofluid-based coolant mechanisms have been promising as well. At a 10 C charging/discharging rate and using hydrofluoric ether as a heat transfer fluid, the cell temperature was maintained at 35–50 °C, which was otherwise 80–90 °C for an air-cooling system. Using ammonia-based coolant, Al-Zareer et al. [117] showed that such BTMS provides a better reduction in cell skin temperature, whereas the skin temperature was <40 °C and the charging and discharging rate was 7.5 C. The Al₂O₃-based nanofluids were used by Huo and Rao [118] as a cooling medium. Due to the high heat capacity of nanofluids, the average cell temperature was found to be decreased by 7%. As compared to nanofluids with flows, a condition on Al₂O₃-based nanofluids with non-circulation was studied by Jilte et al. [119] and the results suggested that the system can perform well for a moderate charge/discharge rate (2 C).

Indirect liquid cooling: The indirect-based liquid cooling avoids any contact of the cell surface to the coolant, thus reducing the possibility of corrosion and reaction, whereas increasing the range of operating temperature for better performance provides better support for the battery pack. In this case, the heat transfer fluids passed through a cold

plate attached or sandwiched to the sides of the cell. Though the passive cooling method can implement better on prismatic cell configuration, the rounder contact supports the transport of better heat from a cylindrical cell [115]. For a prismatic cell configuration, the temperature increment for 4 C discharge rate, the air- and water-based flows in a microchannel can cause a temperature increment of 25 °C and 5 °C, respectively. The results signify a significant decrease in average surface temperature based on indirect liquid cooling [113].

Liquid metals: The application of a liquid-based BTMS could be further improved by the application of liquid metal applications [120,121]. The liquid metal provides a much higher thermal conductivity than the typical water or aqueous ethanol. Generally, aluminum is a preferred choice because of its lightweight and high thermal conductivity. The corrosion due to liquid metal application can be overcome by the anode coloring, which isolates the liquid metal and Al. Another advantage of liquid cooling is electromagnetic driving (EMO) where the change in flow direction can be attained (Figure 21). In addition, these systems required limited maintenance costs and are much more reliable than the liquid-based system as they are applied in a rather simple and robust system. However, as liquid metal has a significantly higher density (approximately six times water), this type of BTMS adds significant weight for the same volume of coolant.

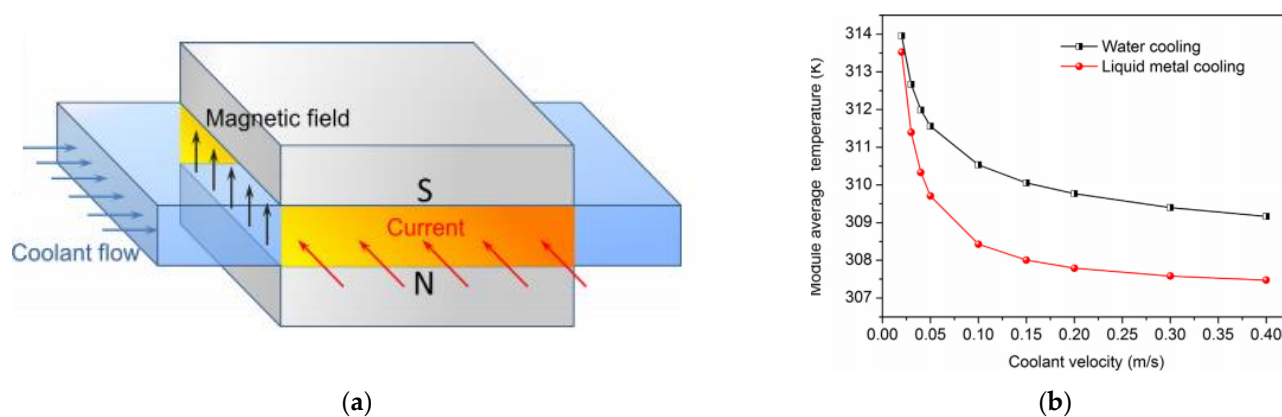


Figure 21. (a) Working principle of an electromagnetic pump (EMP). (b) A comparison of module average temperature between liquid metal cooling and water cooling. Reprinted with permission from [120]. Copyright 2016 Elsevier.

Table 4. Recent developments in liquid-based battery thermal management methods.

Authors	Strategies	Recommendations	Methods
Yu et al. (2005) [122]	Thermal management of PEM fuel cell stack	An earlier model of water and thermal management system was based upon mathematical analysis to attain the optimum result.	Mathematical
Giuliano et al. (2011) [23]	Aluminum cooling plates	At 300 A discharges, the proposed system was able to control the temperature below 50 °C.	Experiment
Jarrett and Kim (2011, 2014) [123,124]	Serpentine- channel shape cooling plate	A serpentine channel shape cooling panel could optimize pressure drop and maximum cell temperature; although, the temperature differential increased. The temperature uniformity was found to be most sensitive to the design operating conditions, especially the heat flux and flow rate.	Numerical simulation

Table 4. Cont.

Authors	Strategies	Recommendations	Methods
Hung et al. (2013) [125]	Nanofluids (Al ₂ O ₃ /water)	For a nanofluidic-based system, the most efficient performance was obtained when nanofluid concentrations were ~0.5%, while the flow rate was significantly lower (0.8 L/min).	Experiment
Bandhaeur et al. (2013) [126]	Passive microchannel phase change system (Liquid R134a)	A new two-phase refrigerant in the microchannel was tested for a passive internal thermal management system. A correlation for the friction factor for such a two-phase system was proposed and tested. With a minimum expense of pumping power, the proposed system can reduce both the cell temperature and the pack temperature differential. At a discharge rate of 1 C, using a flow rate of 0.20 L/min, the maximum temperature rise was less than 27.81 °C, whereas the temperature differential was 0.80 °C after 1 h of discharging, with only 8.69×10^{-6} W pumping power required.	Experiment
Lan et al. (2014) [127]	Mini-channel cooling	Maximum cell temperature and pack temperature differential were lower than 35 °C and 5 °C, respectively.	Numerical simulation
Nieto et al. (2014) [128]	Cold plate	A mini-channel water cooling system was tested for large prismatic cells for the discharge of 1–2 C and operating temperatures of 5–25 °C.	Experiment, numerical simulation
Panchal et al. (2016) [113]	Mini-channel water cooling	In a five cells pack, the Al ₂ O ₃ /water nanofluids decreased the maximum cell temperature and also maintained the temperature uniformity. For a 0.4 volume fraction of nanofluids, a maximum 7% decrease in maximum cell temperature was obtained.	Experiment, numerical simulation
Huo et al. (2014) [118]	Nanofluids (Al ₂ O ₃ /water)	The mini-channel cold plate could attain the optimum operating temperature when the discharge rate was as high as 5 C. The cell temperature (maximum) and the pack temperature differential decreased by 13.3% and 43.3%, respectively.	Numerical simulation
Qian et al. (2014) [129]	Geometries of inlet and outlet flow ducts	The simulation and experimental results at a significantly high discharge (10 A) demonstrate the excellent performance of the hydrogel TMS in decreasing the temperature gain and minimizing the temperature gradient inside the pack. A battery pack equipped with the hydrogel TMS exhibits a reduced capacity fading.	Analytical, numerical simulation
Zhang et al. (2014) [130]	Water-based PAAS (sodium polyacrylate) hydrogel	An oblique alignment of a mini-channel liquid cold plate was applied, where the performance was significantly higher than with the normal liquid cold plate. The proposed structure could keep the maximum surface temperature below the critical limit (50 °C) even for a high thermal load (~1240 W) and a low flow rate (~0.9 L/min).	Experiment, numerical simulation
Jin et al. (2014) [131]	Oblique minichannel liquid cold plate		Experiment, numerical simulation

Table 4. Cont.

Authors	Strategies	Recommendations	Methods
Tong et al. (2015) [132]	Water and coolant plate	The thermal performance of the battery pack could be improved by extending the coolant plate thickness and flow rate. The proposed system could also increase the weight or volume; hence, an optimum design condition is necessary.	Numerical simulation
Huo et al. (2015) [133]	Mini-channel cold plate	The maximum cell temperature decreased if the number of cooling channels increased. The coolant performance could be improved with a water flow lateral to the electrodes. The thermal performance can be enhanced by increasing the flow rate; however, the efficiency could decrease above the optimum operating conditions.	Numerical simulation
Saw et al. (2015) [134]	Liquid cooling	Thermal management systems were analyzed for liquid and air cooling. It was suggested that among various methods available, the direct contact liquid cooling system was more effective in extracting the heat generated in the cell and creating an optimum operating environment for the battery.	Numerical simulation
Smith et al. (2015) [135]	Three sample cooling plate concepts	It was shown that the ideal cooling plate design depends on the anticipated cell heat loss and operating climate, as well as the degree of structural integration within the vehicle.	Experiment
Chen et al. (2016) [136]	Direct liquid, indirect liquid, fin, and air cooling	A 3-dimensional electrochemical–thermal model was applied to evaluate four BTMS (air, direct liquid cooling, indirect liquid cooling, and fin-type) and compared. Maintaining the same average temperature for the air-based method needed two to three times higher energy. However, water/glycol was most efficient in reducing the cell temperature compared to oil, air, or fins.	Numerical simulation
Basu et al. (2016) [137]	Aluminum sheets wrapping/Liquid coolant	The proposed system could reduce the maximum cell temperature below 7 K even at high discharge. In addition, the system was found to be efficient in cooling the pack at low flow rates.	Experiment, numerical simulation
Mondal et al. (2017) [138]	Nanofluids (ethylene glycol, Al ₂ O ₃ , CuO)	Pure H ₂ O-based coolants offered better thermal performance in the form of lower overall temperatures and less temperature gradient. The enrichment with nanoparticles did not have a significant impact on the pack temperature, despite the increase in thermal conductivity.	Numerical simulation
An et al. (2017) [139]	Mini-channel (flow boiling)	The BTMS devised on hydrofluoroether flow boiling in micro-channels could keep temperatures of battery cells around 40 °C and could improve the temperature uniformity in the cell.	Experiment
Gao et al. (2022) [140]	Gradient channel based	Optimally designed gradient channel design can enhance the cooling performance of the BTMS. The proposed design can significantly improve the thermal uniformity in the pack for a lower inlet flow rate.	Experiment, numerical simulation

The water-based BTMS offers a higher rate heat transfer coefficient and rapid convective heat transport. Compared to a conventional air-cooling method, liquid cooling can be compact and space-conserving. At the same time, it can also support the temperature uniformity in the entire pack or an individual cell. However, the system requires careful consideration of the heat exchanger system, free from any water leakage that can cause a safety incident. In addition, due to an extensive duct and pumping system along with water storage, the system would be less cost-effective than the air-based BTMS.

3.3. PCM-Based Thermal Management

PCM-based materials exhibit excellent heat absorption properties utilizing the large latent heat of fusion per unit volume capability that has previously been applied for residential cooling applications, thermal management of electronics, spacecraft thermal management, medical treatment, etc. In addition, a minimum change in volume during the phase change and capability of intermittent or transient heat dissipative capability has been proposed as an efficient method for battery thermal management. Common materials are paraffin, salt hydrates to the recent development of functionalized BioPCM and organic materials. To reduce the thermal runaway conditions and high-temperature gradient within the cell in a battery pack in an air-based system, such a PCM-based system was experimentally and numerically tested for both winter and summer conditions by Khateeb et al. [141] as shown in Figure 22. The setup was applied for a scooter with a 1 h charging cycle. The results from the three cycles were shown in Figure 22b, where the cell inside the pack (Cell-3) exhibits the highest temperature. Recent developments of the phase change BTMS are summarized in Table 5.

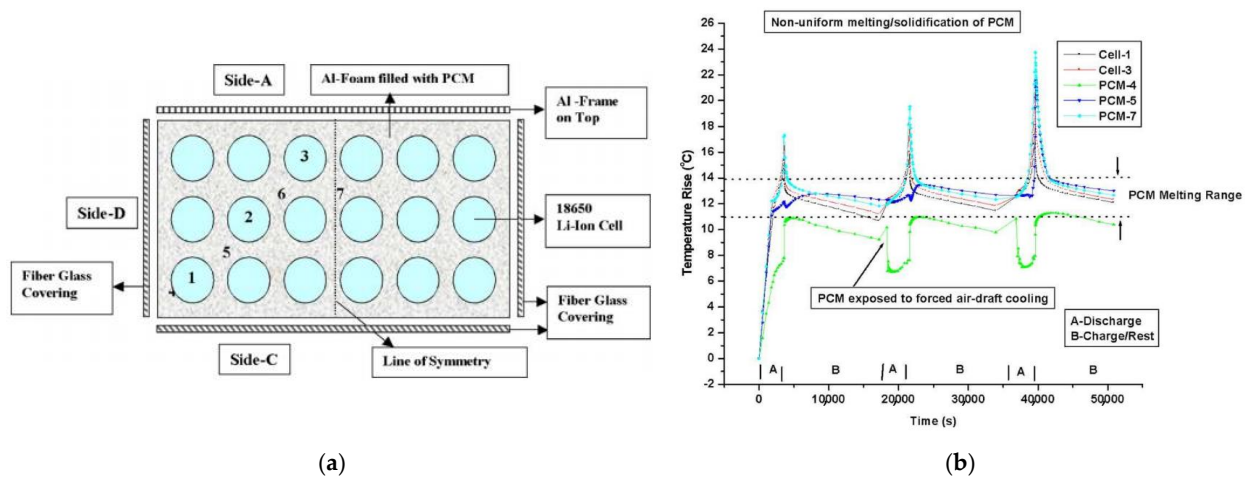


Figure 22. (a) Li-ion battery cell filled with PCM. (b) Temperature rise of Li-ion cells and three different PCMS settings. Reprinted with permission from [142]. Copyright 2004 Elsevier.

Table 5. Recent developments of PCM-based battery thermal management methods.

Authors	Materials	Recommendations	Methods
Hallaj et al. (2000) [143]	Paraffin	A PCM-based BTMS was studied for 18650 cells. Excess heat emitted during discharge could be transferred and stored in the surrounding PCMs, which could heat the cell during charging. As the PCM has a lower melting point, these reverse thermal transport processes were activated when the cell temperature fell below the PCM melting temperature. The PCM-based method is promising in cold climates and space conditions.	Experiment, numerical simulation

Table 5. Cont.

Authors	Materials	Recommendations	Methods
Khateeb et al. (2004) [141]	Composite (Paraffin and Al foam)	The Al foam with PCM could reduce the cell temperature by a maximum of 50% in contrast to the application of any BTMS. PCM methods were used to maintain uniformity in the pack. However, the poor heat conductivity of PCM could decrease the performance of the BTMS. A PCM-based method was tested for paraffin in copper foam by a detailed thermo-electrochemical model.	Experiment, numerical simulation
Qu et al. (2014) [144]	Paraffin and foam	The proposed copper-embedded paraffin foam could significantly reduce the cell temperature within the operating temperature range for a discharge of 3 C, which was not possible by a conventional air-based system.	Numerical simulation
Lin et al. (2014) [145]	Foam Paraffin composite	The proposed foam paraffin composite saturated with PCM materials could achieve a significantly higher thermal performance than the pure PCM-based system. It was also suggested that the growth of porosity and density of pore could increase the cell surface temperature. PCM saturated Polyurethane foam could increase the performance significantly as compared to the dry foam. For example, the use of PCM soaked foam decreased the surface temperature by 7.3 K more than that of dry foam. This method could also enhance the temperate homogeneity in the battery pack.	Experiment
Javani et al. (2014) [146]	Polyurethane foam	PCM saturated Polyurethane foam could increase the performance significantly as compared to the dry foam. For example, the use of PCM soaked foam decreased the surface temperature by 7.3 K more than that of dry foam. This method could also enhance the temperate homogeneity in the battery pack.	Numerical simulation
Hemery et al. (2014) [147]	PCM with air cooling	The wall temperature of a defective cell remains under 60 °C during the failure test. The PCM-can/cell weight ratio is about 46.7%, compared to 28.6% obtained by Khateeb et al. [141].	Experiment
Ling et al. (2015) [148]	PCM with forced air cooling	The combined method can remarkably enhance thermal performance and reduce heat accumulation. The proposed system could also maintain the cell temperature under all cycle conditions (1.5 C and 2 C discharge rates).	Numerical simulation
Wang et al. (2015) [149]	Paraffin and paraffin/aluminum foam	The aluminum foam was used along with paraffin in an attempt to decrease the melting temperature and enhance the temperature uniformity in the PCM system. For the heat flux of 7000 W/m ² and 12,000 W/m ² , the energy storage time of the proposed structure was 73.6% and 74.4%, respectively, for the pure paraffin. Composite PCM (with carbon fibers) was proposed. It was suggested that a composition of 2 mm long carbon fibers and 0.46% (mass fraction) carbon fibers could provide the optimal performance, and the maximum temperature could be reduced by a maximum of 45%.	Numerical simulation
Babapoor et al. (2015) [150]	Composite (Carbon fiber)	Composite PCM (with carbon fibers) was proposed. It was suggested that a composition of 2 mm long carbon fibers and 0.46% (mass fraction) carbon fibers could provide the optimal performance, and the maximum temperature could be reduced by a maximum of 45%.	Numerical simulation

Table 5. Cont.

Authors	Materials	Recommendations	Methods
Shirazi et al. (2015) [151]	Composite (paraffin, graphene, carbon fiber, fullerene)	It was reported that the application of paraffin nanocomposites could be beneficial when the battery undergoes fast and nonstop discharging cycles. A PCM and mini-channel coupled system was proposed. For eight mini-channels and an $8 \times 10^{-4} \text{ kg s}^{-1}$ flow rate, the optimal operating temperature and thermal conductivity for the PCM were 308.15 K and $0.6 \text{ W m}^{-1} \text{ K}^{-1}$, respectively.	Numerical simulation
Rao et al. (2016) [152]	Composite (PCM/mini-channel coupled)	In addition, for the same operating conditions, when the maximum temperature of the PCM-based BTMS was 335.4 K, the maximum temperature for the proposed system was 320.6 K. The proposed phase changed microcapsule (n-octadecane enriched	Numerical simulation
Yang et al. (2016) [153]	Phase change microcapsule	polymethylmethacrylate shell) could improve the thermal property significantly. The addition of silicon nitride could enhance the thermal conductivity by 56.8%. Fin structures (with an optimum number of	Experiment
Sun et al. (2016) [154]	Fin structures in PCM	1 and 8) could maintain the cell temperature within the operating range even for a heat generation of 20 W. Nickel foam fused paraffin composite could significantly enhance thermal performance. Under 2 C discharge rate, the proposed structure reduces the cell temperature by 31% and 24% when compared with natural convection and pure PCM.	Numerical simulation
Hussain et al. (2016) [155]	Nickel foam–paraffin composite	A set of PCMS with Al foam composite was tested. Gallium as PCM could enhance the surface temperature uniformity and discharge time. Whereas, AL foam with Octadecane could achieve a significant uniformity in surface temperature.	Experiment
Alipanah et al. (2016) [156]	Pure gallium and octadecane–Al foam composite	A metal matrix–PCM composite was recommended as a better substitute than the nanoparticle PCM composite. In addition, among different nanoparticles, composite containing Ag nanoparticles predicted the best thermal performance. Carbon fiber-based composite was suggested to enhance the temperature uniformity in the pack. In addition, carbon fiber-based composite could enhance the thermal conductivity by an average of 105%.	Numerical simulation
Karimi et al. (2016) [157]	Metal matrix and nanoparticles with PCM	Graphite-based composite is proposed to be effective and could increase the thermal conductivity by up to $70 \text{ W m}^{-1} \text{ K}^{-1}$.	Experiment
Samimi et al. (2016) [158]	Composite (Carbon fiber)		Numerical simulation
Malik et al. (2016) [159]	Composite (Graphite)		Numerical simulation

Table 5. Cont.

Authors	Materials	Recommendations	Methods
Jiang et al. (2016) [160]	Paraffin (RT44HC)/expanded graphite (EG) composite	EG incorporation dramatically enhanced the thermal conductivity of the composite. Hence, the cell temperature could be remarkably decreased, whereas the optimum mixture was proposed as a composite with 16–20 wt.% EG.	Numerical simulation
Lv et al. (2016) [161]	Paraffin (PA) and low-density polyethylene (LDPE)	The PCM composite kept the maximum cell temperature below 50 °C and reduced the temperature differential by 5 °C for a battery pack working under the safety temperature of 50 °C and up to a very high discharge rate (3.5 C).	Experiment
Wu et al. (2016) [162]	Composite (Paraffin with copper mesh)	Copper mesh embedded PCM could significantly enhance the temperature uniformity than the pure PCM. These methods were recommended to be more effective in harsh working conditions.	Experiment
Azizi et al. (2016) [163]	Composite (Poly Ethylene Glycol with aluminum wire mesh)	The PCM and use of aluminum wire mesh in the cell spacing reduced the cell skin temperatures at ambient conditions by a maximum of 26% at a discharge rate of 3 C. It was suggested that PCMs with too low or high melting temperatures deteriorate the performance, and a melting temperature of 40–45 °C could give the best thermal performance. As expected, the discharge time and rates decrease the temperature uniformity. Conversely, the proposed method could maintain the maximum temperature differential at 5 °C at a discharge rate of 2 C.	Numerical simulation
Ling et al. (2014) [148]	EG (Ethylene Glycol) based PCM	The proposed technique was recommended with liquid cooling, which could keep the maximum cell temperature beneath 50 °C for a discharge rate of 3 C. A shape memory-based thermal regulator was proposed that could adjust its thermal conductivity depending on the temperature. This regulator was found to increase the battery capacity by three times at –20 °C compared to a conventional BTMS with no thermal regulation function. This method was recommended for extreme environmental conditions.	Experiment, numerical simulation
Wu et al. (2017) [164]	Heat pipe-assisted phase change material		Experiment
Hao et al. (2018) [165]	Shape memory alloy-based passive interfacial thermal regulator		Experiment

The PCM-based system provides as many benefits as a water-based system in terms of heat transfer coefficient while removing a few of the major drawbacks of the water-based system, such as requirements for extensive water circulation pipes, pumping and storage unit, and insulation for any possible leakage. The PCM system also provides good benefits for both active and passive BTMS applications during high-temperature operations. However, the PCM-based system offers the least degree of benefit when heating of the cell is necessary without installing any external heating units. The PCM-based modules are less cost-effective than the air-based system and have a higher operating cost in terms of maintenance and reinstallations.

3.4. In Situ Thermal Management

In situ battery thermal management has been a new technology, and the cost to implement it typically is high compared to other methods. These methods are typically selected when heating/cooling time needs to be minimized. These strategies serve better at the material, cell, and system-level considerations (Figure 23). The conventional thermal management concept relies on external interference and has safety limitations, especially in a cold climate ($<20\text{ }^{\circ}\text{C}$) and arid weather ($>60\text{ }^{\circ}\text{C}$). At these temperatures, the safety of Li-ion batteries intrinsically relies on electrode materials and solid-electrolyte interphase [166].

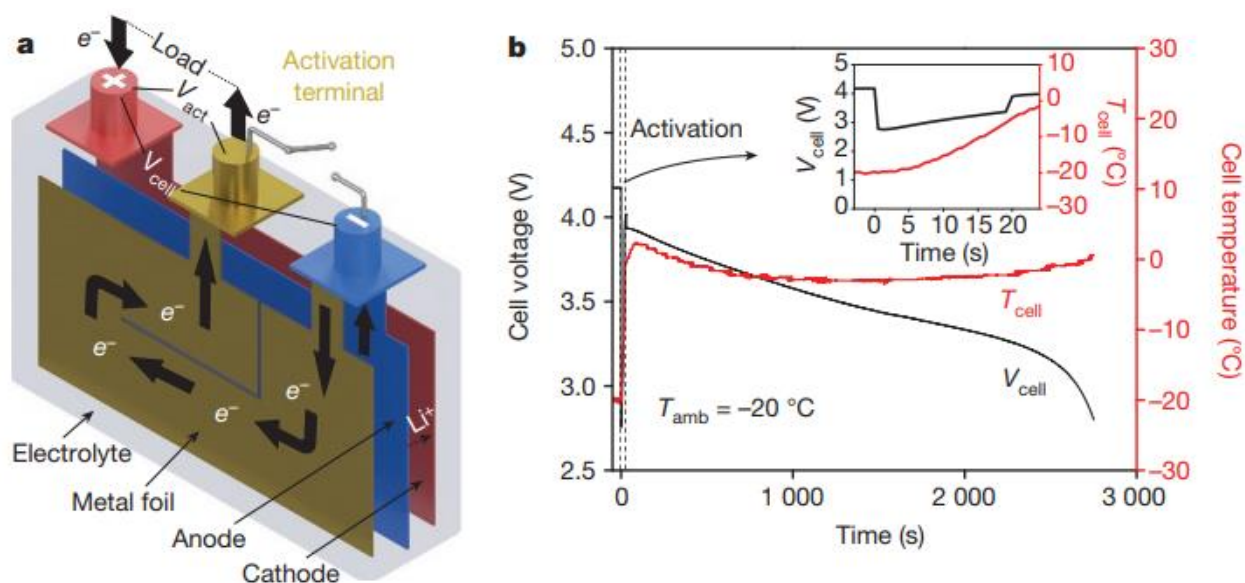


Figure 23. (a) In situ thermal management concept designed on an internally installed metal foil that can produce heat at low temperature using controlled self-heating. (b) Transient profile of temperature and discharge voltage during the activation. Reprinted with permission from [167]. Copyright 2016 Nature.

In Table 6, it is evident that in situ thermal management techniques can be very effective; however, it is not sufficient to substitute the external cooling system. In most cases, an effective thermal management system can be achieved through both external forced systems and internal thermal systems. As a significant portion of power has been spent on running the cooling system, the internal-based system can significantly reduce operating costs.

Table 6. Recent developments of in situ battery thermal management methods.

Authors	Strategies	Recommendations	Methods
Zhang et al. (2002) [168]	Electrolytes modification	In comparison to an LiPF_6 -based electrolyte, the electrolyte made of LiBF_4 salt has lower conductivity, but it provides an improved low-temperature performance. LiBF_4 can be used to formulate an electrolyte that can increase the allowable temperature limit of the battery (-40 to $60\text{ }^{\circ}\text{C}$).	Experiment
Vlahinos et al. (2002) [169]	Internal core heating external/internal jacket heating.	Four different cooling strategies were compared for cold climates. An electric heating system was recommended for faster heating. Conversely, internal core heating was recommended to obtain uniform heating.	Numerical simulation

Table 6. Cont.

Authors	Strategies	Recommendations	Methods
Viswanathan et al. (2009) [170]	Entropy change	The effects of entropy generation in various electrodes and a cell were calculated, which represent a substantial proportion of the overall heat production. It was also indicated that an appropriate combination of cathode/anode material could abate the reversible heating.	Experiment
Fleckenstein et al. (2011) [171]	Temperature gradient	The current distribution caused by the temperature gradient can intensify the unequal aging behavior in the cell. For LiCoO ₂ cells, capacity fade grows with the square root of the current magnitude (Ning et al. [172]). In addition, the increased charge throughout warmer cell regions is expected to induce locally accelerated capacity fading.	Experiment, numerical simulation
Doughty et al. (2012) [173]	Self-heating	It was indicated that self-heating could improve cathode stability and reduce the peak heating rate. Consequently, this stability could increase the temperature necessary for a thermal runaway.	Review
Shi et al. (2014) [174]	Surface modification	La _{0.7} Sr _{0.3} Mn _{0.7} Co _{0.3} O ₃ coating facilitates lithium-ion diffusion at the interface, which is also beneficial to improve the rate capability.	Experiment
Zhao et al. (2015) [175]	Electrode modification	The interface should be modified with a conductive adhesive pad or paste to reduce the thermal resistance.	Review
Wang et al. (2016) [167]	Metal foil insert (Figure 23)	It was recommended that the proposed cell with a metal foil insert could raise the temperature self-sufficiently, even if the cell temperature drops below 0 °C.	Experiment
Loges et al. (2016) [176]	Specific heat capacities	The largest temperature dependency was observed for the separators, while the specific heat capacities of the considered electrolytes exhibit the lowest increase with temperature. The porosity and coating thickness has a superimposed effect on the specific heat capacities of anode and cathode.	Experiment, numerical simulation
Yang et al. (2018) [177]	Fast charging	Charging at a higher temperature avert Li-plating. Therefore, high-temperature cell operation was recommended as a method to increase the life of the cell.	Experiment

3.5. Heat Pipes and Thermoelectric Modules

Heat pipes have increasing applications in electronic components comprising CPUs of phones and computers, LED, laser generators, spacecraft, solar energy collectors, etc. [178]. In the most common heat pipe-based BTMS, the evaporator portion can be generally coupled with cell surfaces, and the condenser section is attached to the cooling components (Figure 24). These types of thermal management units could replace air and water cooling systems and significantly simplify the design [179]. This type of system coincides with the concept of integrated thermal management (e.g., regeneration in the Brayton cycle). Temperature control could be achieved using a thermoelectric element and a heat pipe. In the conventional air-cooled system, the unit uses cabin air, which increases the load for the air conditioning unit and decreases the vehicle's energy efficiency. Such uses of cabin air are unnecessary for heat pipes, thermoelectric modules, and many in situ thermal management systems, increasing the overall efficiency of the systems. The thermoelectric modules can

be implemented in a closed type system preventing an introduction of water from being introduced from a cooling air inlet/out, which can prevent a safety incident. Another benefit of the system is that it can increase the driving distance and cost distance, by removing the cooling channel, cooling duct, fan, and air-conditioning unit, thereby simplifying the system and reducing the weight of the thermal management unit. The heat pipe system offers an excellent advantage in battery thermal management and thermal runaway prevention due to its low thermal resistance, high heat transfer, and isothermal thermal transport. Hence, recently a significant amount of effort has been dedicated to the advancement of heat pipe for BTM covering major challenges and design configurations [164,178,180–194].

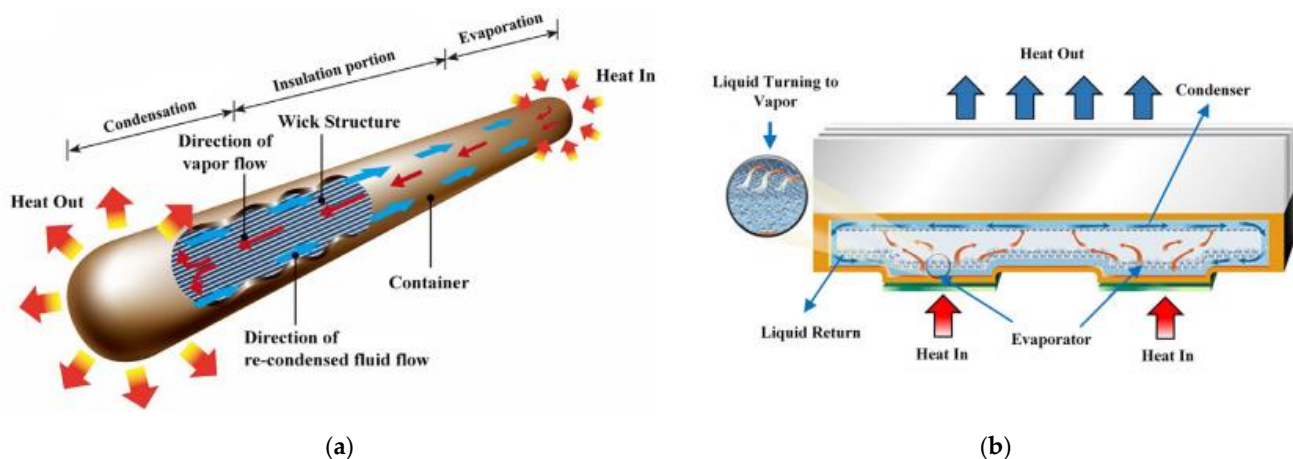


Figure 24. (a) Working principle of a standard tubular heat pipe. (b) 2D schematic diagram of a standard heat pipe. Reprinted with permission from [195]. Copyright 2008 Elsevier.

The heat pipe-based system can provide an efficient method of solution for high-power-density cells and is deemed to be efficient in smaller scale and precise solutions, which have mostly been covered in the literature. However, the viability of such systems at pack-level consideration requires further investigation. Moreover, one of the key challenges of a heat pipe-based system is the presence of a bottleneck between the evaporator and the condenser resulting in a temperature gradient across the width of the cell [196]. In this sense, a heat pipe-based system can be coupled with air, liquid, or PCM-based systems to further enhance and optimize the performance of the BTMS for high-power applications [197–201].

4. Conclusions

In this study, we attempt to answer the question of battery thermal management in EVs and HEVs using both theoretical and experimental or operational practices. Covering multifaceted factors and complexities of BTMS in EVs or HEVs is an unattainable quest within the context of the article. Therefore, the review has been organized with two major aspects (theory and practices) for an overall perspective of the concept of battery thermal management. From the analysis of processes and scales of cell hierarchy, key theoretical concepts necessary to understand the thermal management from cell to pack level were presented using the mathematical explanation. For example, a significant temperature gradient in the cell can cause uneven aging and electrode thermal instability at high Biot number conditions, thus signifying the importance of a spatial-resolution lumped thermal model. Similarly, the equivalent circuit model could also apply to efficiently estimate the core and skin temperature of the cell depending on uneven heat generation. The prediction of core temperature, especially for high power density cells, would be much more effective and would give precise feedback to the control system to better estimate the SOC [202,203] and optimize the flow system [112,204], necessary to keep the cell temperature under control and improve the temperature uniformity within the pack.

The study also listed major practices of thermal management and discussed their performances, reference works, and findings. The thermal management practices used

in Li-ion battery-powered electric vehicles may be reasonably considered or used as a reference point for future fuel cell-powered electric vehicles [205,206]. In this study, we emphasized the difference between those methods (air/liquid/PCM/in situ/heat pipes) in a tabulated format. While the methodologies described in the literature cannot explicitly conclude the optimum method of battery thermal management, these should be determined by the cell heat generation rate, FUDS cycle, and expected life cycle. Comparisons of the aforementioned BTM technologies along with their applicability, reliability, and adaptability are summarized in Table 7. The assessment in Table 7 suggested that the selection of the BTM cannot be drawn solely based on operating efficiency, but it is subjugated by weather conditions and also by particular applications. For example, the performance of high-end or stock vehicles could be optimized through a coupled BTMS approach, such as heat pipes/PCM/in situ methods with convective air/liquid flows. Whereas satisfactory performance could be realized through the air or liquid cooling methods in regular vehicles operating in moderate climates. To design an effective thermal management system, the emphasis should also be given to the energy efficiency ratio (EER) as defined by the ratio of the cooling capacity of the system and the total input power of the cooling system. New paradigms and practices of BTMS research shall encompass two additional functionalities, such as minimization of lithium plating and maximization of diffusion rates while keeping the temperature within the minimum operating range. At the current state of the art, such enhancements can be envisioned through the combination of in situ technique and external air/water-cooling. Inevitably the progress in material science is essential for an effective in situ method to yield high-temperature resistance and highly diffusive materials for cathode, anode, and solvent, allowing the transport of heat from the cell core to the surface in an effective means. Consequently, an effective air/water-cooling method can be applied to keep the cell within the operating range, which could be further enhanced by passive methods (PCM, heat pipes). These new technologies (heat pipes/PCM/in situ) are still in the research phase and may be seen in EVs and HEVs in the upcoming years. Conversely, mathematical and numerical modeling along with IoT-cloud-based infrastructure could further optimize thermal management efficiency and energy consumption.

Table 7. Comparative analysis of different battery thermal management practices.

BTM Approaches	Major Advantages	Major Drawbacks	Cost, Reliability, and Adaptability
Air-based	<ul style="list-style-type: none"> - the most convenient and cost-effective method to implement - can be applied in any operating conditions, however, performance can deteriorate - usability of cabin air - less energy consumption - low operating costs - relatively safer than other methods 	<ul style="list-style-type: none"> - less efficient - more effective in cooling than heating uses - not effective in high power density cells - not effective in extreme weather - temperature nonuniformity in the pack could detriment the overall performance 	<ul style="list-style-type: none"> - cost-effective - adaptable and reliable - Nissan Leaf, Toyota Prius
Liquid-based	<ul style="list-style-type: none"> - enhance thermal uniformity in the pack - moderate operating costs - depending on fluids and phase change fluids, a significant improvement in performance can be achieved - can be coupled with other BTMS - as a liquid-based system is an established method of thermal management for many applications, it can be implemented using existing technology 	<ul style="list-style-type: none"> - required insulation, leakage may cause a short circuit - parasitic power losses - additional energy consumption - not applicable in all weather conditions as any phase change phenomenon in extreme climate conditions will significantly deteriorate the performance 	<ul style="list-style-type: none"> - adaptable and reliable - GM Volt, Tesla Model S

Table 7. Cont.

BTM Approaches	Major Advantages	Major Drawbacks	Cost, Reliability, and Adaptability
PCM	<ul style="list-style-type: none"> - no external energy input (passive method) consumption for pure PCM-based method - fast control of the temperature - suitable in harsh weather (overheating, freezing, etc.) - enhance temperature uniformity - can be coupled with an air or liquid-based system for further improvements in performance 	<ul style="list-style-type: none"> - still in the research phase - stability of the PCM materials could be an issue - more effective in cooling functionality and development of effective PCM materials that are highly thermally conductive and flame retardant 	<ul style="list-style-type: none"> - has not been implemented in running EVs
In situ	<ul style="list-style-type: none"> - no external energy input - effective elimination of Li-plating - effective in heating (especially cold start) - reduction in pack size and application in confined space - can be coupled with an air or liquid-based system for further improvements in performance 	<ul style="list-style-type: none"> - higher manufacturing costs due to cathode/anode/surface modification - relied on the development of advanced materials 	<ul style="list-style-type: none"> - has not been implemented in running EVs
Heat pipes	<ul style="list-style-type: none"> - no external energy input - applicable to high power density cells - improve temperature uniformity in the pack - reduction in a pack size - can be applied intermittently to save energy consumption - can be coupled with an air, liquid, or PCM-based system for further improvements in performance 	<ul style="list-style-type: none"> - not applied in large scale application - may increase nonuniformity in cell temperature distribution - not effective in high power density cells - the running costs would be significantly high 	<ul style="list-style-type: none"> - has not been implemented in running EVs

Thermal management of batteries is the key element of energy management and directly or indirectly influences the performance of other components of EVs and HEVs, including energy storage units, management of supercapacitors, the realization of fast charging and wireless charging, grid integration, control strategies, alternative and renewable energy sources, cooperative charging, etc. [207–216]. As it is envisioned that the hub drive powertrain would be the direction of future powertrain design, intelligent and optimized energy and thermal management would require for such hub driven or conventional EVs and HEVs. Theoretical development in these new sectors has progressed parallelly and conceptualized in the literature focusing on efficient energy storage, driving range improvement, and vehicle safety (e.g., thermal runaway). Examples include integrated and optimized energy and thermal management methods [217–219], an intelligent control algorithm for hub and distributed drive vehicles [220,221], and decentralized energy management strategies for islanded microgrids [222,223]. Integration of these multilayered developments in existing, or future BTMS would essentially benefit the thermal management practices.

Funding: This research was funded by Army Research Laboratory contract number W911NF2020134.

Conflicts of Interest: The authors declare no conflict of interest.

References

1. Pistoia, G. *Lithium-Ion Batteries: Advances and Applications*, 1st ed.; Elsevier: Amsterdam, The Netherlands, 2014.
2. Linden, D.; Reddy, T.B. *Handbook of Batteries*, 3rd ed.; McGraw-Hill: New York, NY, USA, 2002.
3. Pistoia, G.; Liaw, B. *Behaviour of Lithium-Ion Batteries in Electric Vehicles: Battery Health, Performance, Safety, and Cost*; Green Energy and Technology: Cham, Switzerland, 2018.
4. Scrosati, B.; Garche, J.; Tillmetz, W. *Advances in Battery Technologies for Electric Vehicles*, 1st ed.; Woodhead Publishing: Cambridge, UK, 2015.
5. Dinçer, I.; Hamut, H.S.; Javani, N. *Thermal Management of Electric Vehicle Battery Systems*; Wiley: Hoboken, NJ, USA, 2017.
6. Goodenough, J.B. Theory of the Role of Covalence in the Perovskite-Type Manganites [La, M(II)]MnO₃. *Phys. Rev.* **1955**, *100*, 564–573. [[CrossRef](#)]
7. Mizushima, K.; Jones, P.C.; Wiseman, P.J.; Goodenough, J.B. Li_xCoO₂ (0 < x ≤ 1): A new cathode material for batteries of high energy density. *Mater. Res. Bull.* **1980**, *15*, 783–789.
8. Goodenough, J.B.; Schuman, B. Manganese Oxides as Battery Cathodes. In *Proceedings Symposium on Manganese Dioxide Electrode: Theory and Practice for Electrochemical Applications*; Re Electrochem. Soc.: Hoboken, NJ, USA, 1985; Volume 85–84, pp. 77–96.
9. Ohzuku, T.; Brodd, R.J. An overview of positive-electrode materials for advanced lithium-ion batteries. *J. Power Sources* **2007**, *174*, 449–456. [[CrossRef](#)]
10. Lee, S.; Kwon, G.; Ku, K.; Yoon, K.; Jung, S.-K.; Lim, H.-D.; Kang, K. Recent Progress in Organic Electrodes for Li and Na Rechargeable Batteries. *Adv. Mater.* **2018**, *30*, e1704682. [[CrossRef](#)] [[PubMed](#)]
11. Peng, L.; Shen, X.; Dai, J.; Wang, X.; Zeng, J.; Huang, B.; Li, H.; Zhang, P.; Zhao, J. Three-Dimensional Coating Layer Modified Polyolefin Ceramic-Coated Separators to Enhance the Safety Performance of Lithium-Ion Batteries. *J. Electrochem. Soc.* **2019**, *166*, A2111–A2120. [[CrossRef](#)]
12. Chen, X.; Chen, S.; Lin, Y.; Wu, K.; Lu, S. Multi-functional ceramic-coated separator for lithium-ion batteries safety tolerance improvement. *Ceram. Int.* **2020**, *46*, 24689–24697. [[CrossRef](#)]
13. Teki, R.; Datta, M.K.; Krishnan, R.; Parker, T.; Lu, T.-M.; Kumta, P.N.; Koratkar, N. Nanostructured Silicon Anodes for Lithium Ion Rechargeable Batteries. *Small* **2009**, *5*, 2236–2242. [[CrossRef](#)]
14. Freitag, S.; Berger, C.; Gelb, J.; Zeiss, C.; Weisenberger, C.; Berthaler, T. Scanning Electron Microscopy of Lithium-Ion Battery Components. Available online: <https://blogs.zeiss.com/microscopy/en/2016> (accessed on 19 May 2022).
15. Wang, Q.; Ping, P.; Zhao, X.; Chu, G.; Sun, J.; Chen, C. Thermal runaway caused fire and explosion of lithium ion battery. *J. Power Sources* **2012**, *208*, 210–224. [[CrossRef](#)]
16. Liu, H.; Wei, Z.; He, W.; Zhao, J. Thermal issues about Li-ion batteries and recent progress in battery thermal management systems: A review. *Energy Convers. Manag.* **2017**, *150*, 304–330. [[CrossRef](#)]
17. Feng, X.; Ren, D.; He, X.; Ouyang, M. Mitigating Thermal Runaway of Lithium-Ion Batteries. *Joule* **2020**, *4*, 743–770. [[CrossRef](#)]
18. Wu, Y.-S.; Pham, Q.-T.; Yangabg, C.C.; Chernd, C.S.; Babulal, L.M.; Seenivasana, M.; Brunklaus, G.; Plackee, T.; Hwangd, B.J.; Winter, M. Study of electrochemical performance and thermal property of LiNi_{0.5}Co_{0.2}Mn_{0.3}O₂ cathode materials coated with a novel oligomer additive for high-safety lithium-ion batteries. *Chem. Eng. J.* **2020**, *405*, 126727. [[CrossRef](#)]
19. Friesen, A.; Hildebrand, S.; Horsthemke, F.; Börner, M.; Klöpsch, R.; Niehoff, P.; Schappacher, F.M.; Winter, M. Al₂O₃ coating on anode surface in lithium ion batteries: Impact on low temperature cycling and safety behavior. *J. Power Sources* **2017**, *363*, 70–77. [[CrossRef](#)]
20. Mahmoud, A.; Saadoune, I.; Lippens, P.-E.; Chamas, M.; Hakkou, R.; Amarilla, J.M. The design and study of new Li-ion full cells of LiCo₂/3Ni₁/6Mn₁/6O₂ positive electrode paired with MnSn₂ and Li₄Ti₅O₁₂ negative electrodes. *Solid State Ionics* **2017**, *300*, 175–181. [[CrossRef](#)]
21. Zinth, V.; von Lüders, C.; Hofmann, M.; Hattendorff, J.; Buchberger, I.; Erhard, S.; Rebelo-Kornmeier, J.; Jossen, A.; Gilles, R. Lithium plating in lithium-ion batteries at sub-ambient temperatures investigated by in situ neutron diffraction. *J. Power Sources* **2014**, *271*, 152–159. [[CrossRef](#)]
22. Xu, J.; Chao, J.; Li, T.; Yan, T.; Wu, S.; Wu, M.; Zhao, B.; Wang, R. Near-Zero-Energy Smart Battery Thermal Management Enabled by Sorption Energy Harvesting from Air. *ACS Central Sci.* **2020**, *6*, 1542–1554. [[CrossRef](#)]
23. Giuliano, M.R.; Advani, S.G.; Prasad, A.K. Thermal analysis and management of lithium–titanate batteries. *J. Power Sources* **2011**, *196*, 6517–6524. [[CrossRef](#)]
24. Ji, Y.; Wang, C.Y. Heating strategies for Li-ion batteries operated from subzero temperatures. *Electrochim. Acta* **2013**, *107*, 664–674. [[CrossRef](#)]
25. Jaguemont, J.; Boulon, L.; Dube, Y.; Martel, F. Thermal Management of a Hybrid Electric Vehicle in Cold Weather. *IEEE Trans. Energy Convers.* **2016**, *31*, 1110–1120. [[CrossRef](#)]
26. Waldmann, T.; Hogg, B.-I.; Wohlfahrt-Mehrens, M. Li plating as unwanted side reaction in commercial Li-ion cells—A review. *J. Power Sources* **2018**, *384*, 107–124. [[CrossRef](#)]
27. Feng, X.; Ouyang, M.; Liu, X.; Lu, L.; Xia, Y.; He, X. Thermal runaway mechanism of lithium ion battery for electric vehicles: A review. *Energy Storage Mater.* **2017**, *10*, 246–267. [[CrossRef](#)]
28. Hosseinzadeh, E.; Genieser, R.; Worwood, D.; Barai, A.; Marco, J.; Jennings, P. A systematic approach for electrochemical-thermal modelling of a large format lithium-ion battery for electric vehicle application. *J. Power Sources* **2018**, *382*, 77–94. [[CrossRef](#)]

29. Murashko, K. *Thermal Modelling of Commercial Lithium-Ion Batteries*; Lappeenranta University of Technology: Lappeenranta, Finland, 2016.
30. Waldmann, T.; Scurtu, R.-G.; Richter, K.; Wohlfahrt-Mehrens, M. 18650 vs. 21700 Li-ion cells—A direct comparison of electrochemical, thermal, and geometrical properties. *J. Power Sources* **2020**, *472*, 228614. [[CrossRef](#)]
31. Murray, V.; Hall, D.S.; Dahn, J.R. A Guide to Full Coin Cell Making for Academic Researchers. *J. Electrochem. Soc.* **2019**, *166*, A329–A333. [[CrossRef](#)]
32. Quinn, J.B.; Waldmann, T.; Richter, K.; Kasper, M.; Wohlfahrt-Mehrens, M. Energy Density of Cylindrical Li-Ion Cells: A Comparison of Commercial 18650 to the 21700 Cells. *J. Electrochem. Soc.* **2018**, *165*, A3284–A3291. [[CrossRef](#)]
33. Battery-Experts-Forum. Available online: <https://www.battery-experts-forum.com/index.php/en/> (accessed on 19 May 2022).
34. Batteries in a Portable World. Available online: <https://batteryuniversity.com/> (accessed on 19 May 2022).
35. Tarascon, J.-M.; Armand, M. Issues and challenges facing rechargeable lithium batteries. *Nature* **2001**, *414*, 359–367. [[CrossRef](#)] [[PubMed](#)]
36. Mahamud, R.; Park, C. Reciprocating air flow for Li-ion battery thermal management to improve temperature uniformity. *J. Power Sources* **2011**, *196*, 5685–5696. [[CrossRef](#)]
37. Mahamud, R. *Advanced Battery Thermal Management for Electrical-Drive Vehicles Using Reciprocating Cooling Flow and Spatial-Resolution, Lumped-Capacitance Thermal Model*; University of Nevada Reno: Reno, NV, USA, 2017.
38. Mahamud, R.; Park, C. Spatial-resolution, lumped-capacitance thermal model for cylindrical Li-ion batteries under high Biot number conditions. *Appl. Math. Model.* **2013**, *37*, 2787–2801. [[CrossRef](#)]
39. Mahamud, R.; Park, C. Spatial-Resolution, Lumped-Capacitance Thermal Model for Battery Power Cycle Analysis. In Proceedings of the SAE 2011 World Congress & Exhibition, Detroit, MI, USA, 12 April 2011.
40. Liaw, B.Y.; Nagasubramanian, G.; Jungst, R.G.; Doughty, D.H. Modeling of lithium ion cells? A simple equivalent-circuit model approach. *Solid State Ionics* **2004**, *175*, 835–839. [[CrossRef](#)]
41. Moss, P.L.; Au, G.; Plichta, E.J.; Zheng, J.P. An Electrical Circuit for Modeling the Dynamic Response of Li-Ion Polymer Batteries. *J. Electrochem. Soc.* **2008**, *155*, A986–A994. [[CrossRef](#)]
42. Gan, Y.; Wang, J.; Liang, J.; Huang, Z.; Hu, M. Development of thermal equivalent circuit model of heat pipe-based thermal management system for a battery module with cylindrical cells. *Appl. Therm. Eng.* **2020**, *164*, 114523. [[CrossRef](#)]
43. Richardson, R. *Impedance-Based Battery Temperature Monitoring*; University of Oxford: Oxford, UK, 2016.
44. Richardson, R.R.; Zhao, S.; Howey, D.A. On-board monitoring of 2-D spatially-resolved temperatures in cylindrical lithium-ion batteries: Part I. Low-order thermal modelling. *J. Power Sources* **2016**, *326*, 377–388. [[CrossRef](#)]
45. Tran, M.; Panchal, S.; Chauhan, V.; Brahmhatt, N.; Mevawalla, A.; Fraser, R.; Fowler, M. Python-based scikit-learn machine learning models for thermal and electrical performance prediction of high-capacity lithium-ion battery. *Int. J. Energy Res.* **2021**, *46*, 786–794. [[CrossRef](#)]
46. Afzal, A.; Bhutto, J.K.; Alrobaian, A.; Kaladgi, A.R.; Khan, S.A. Modelling and Computational Experiment to Obtain Optimized Neural Network for Battery Thermal Management Data. *Energies* **2021**, *14*, 7370. [[CrossRef](#)]
47. Park, C.-W.; Jaura, A.K. Transient Heat Transfer of 42V Ni-MH Batteries for an HEV Application. *SAE Trans.* **2002**, *111*, 803–808.
48. Liu, Z.; Wang, Y.; Zhang, J.; Liu, Z. Shortcut computation for the thermal management of a large air-cooled battery pack. *Appl. Therm. Eng.* **2014**, *66*, 445–452. [[CrossRef](#)]
49. Liu, R.; Chen, J.; Xun, J.; Jiao, K.; Du, Q. Numerical investigation of thermal behaviors in lithium-ion battery stack discharge. *Appl. Energy* **2014**, *132*, 288–297. [[CrossRef](#)]
50. Nieto, N.; Diaz, L.; Gastelurrutia, J.; Alava, I.; Blanco, F.; Ramos, J.C.; Rivas, A. Thermal Modeling of Large Format Lithium-Ion Cells. *J. Electrochem. Soc.* **2012**, *160*, A212–A217. [[CrossRef](#)]
51. Ratnakumar, B.; Smart, M.; Whitcanack, L.; Ewell, R. The impedance characteristics of Mars Exploration Rover Li-ion batteries. *J. Power Sources* **2006**, *159*, 1428–1439. [[CrossRef](#)]
52. Sato, N. Thermal behavior analysis of lithium-ion batteries for electric and hybrid vehicles. *J. Power Sources* **2001**, *99*, 70–77. [[CrossRef](#)]
53. Li, Y.; Zhou, Z.; Wu, W.-T. Three-Dimensional Thermal Modeling of Internal Shorting Process in a 20Ah Lithium-Ion Polymer Battery. *Energies* **2020**, *13*, 1013. [[CrossRef](#)]
54. Rizk, R.; Louahlia, H.; Gualous, H.; Schaetzel, P. Experimental analysis and transient thermal modelling of a high capacity prismatic lithium-ion battery. *Int. Commun. Heat Mass Transf.* **2018**, *94*, 115–125. [[CrossRef](#)]
55. Al Hallaj, S.; Venkatchalapathy, R.; Prakash, J.; Selman, J.R. Entropy Changes Due to Structural Transformation in the Graphite Anode and Phase Change of the LiCoO₂ Cathode. *J. Electrochem. Soc.* **2000**, *147*, 2432. [[CrossRef](#)]
56. Motloch, C.G.; Christophersen, J.P.; Belt, J.R.; Wright, R.B.; Hunt, G.L.; Sutula, R.A.; Duong, T.; Tartamella, T.J.; Haskins, H.J.; Miller, T.J. High-Power Battery Testing Procedures and Analytical Methodologies for HEV's. *SAE Trans.* **2002**, *111*, 797–802.
57. Srinivasan, V.; Wang, C.Y. Analysis of Electrochemical and Thermal Behavior of Li-Ion Cells. *J. Electrochem. Soc.* **2002**, *150*, A98–A106. [[CrossRef](#)]
58. Thomas, K.E.; Bogatu, C.; Newman, J. Measurement of the Entropy of Reaction as a Function of State of Charge in Doped and Undoped Lithium Manganese Oxide. *J. Electrochem. Soc.* **2001**, *148*, A570–A575. [[CrossRef](#)]
59. Smith, K.; Wang, C.-Y. Solid-state diffusion limitations on pulse operation of a lithium ion cell for hybrid electric vehicles. *J. Power Sources* **2006**, *161*, 628–639. [[CrossRef](#)]

60. Zukauskas, A.; Ulinskas, R. *Heat Transfer in Tube Banks in Crossflow*; Hemisphere Publishing: New York, NY, USA, 1988.
61. Whitaker, S. Forced convection heat transfer correlations for flow in pipes, past flat plates, single cylinders, single spheres, and for flow in packed beds and tube bundles. *AIChE J.* **1972**, *18*, 361–371. [[CrossRef](#)]
62. Frank, P.; Incropera, D.P.D.; Theodore, L.; Adrienne, S.B. *Lavine Introduction to Heat Transfer*; Wiley & Sons, Inc.: New York, NY, USA, 2007.
63. Gaddis, E.S.; Gnielinski, V. Pressure Drop in Cross Flow across Tube Bundles. *Int. Chem. Eng.* **1985**, *25*, 1–15.
64. Cotta, R.M. Improved lumped-differential formulation of diffusion problems. In *Modeling of Engineering Heat Transfer Phenomena*; Sunden, B.M.F., Ed.; Computational Mechanics Publications: Southampton, UK, 1999; Volume 2.
65. Verbrugge, M.W.; Conell, R.S. Electrochemical and Thermal Characterization of Battery Modules Commensurate with Electric Vehicle Integration. *J. Electrochem. Soc.* **2002**, *149*, A45–A53. [[CrossRef](#)]
66. Lin, X.; Perez, H.E.; Mohan, S.; Siegel, J.; Stefanopoulou, A.G.; Ding, Y.; Castanier, M.P. A lumped-parameter electro-thermal model for cylindrical batteries. *J. Power Sources* **2014**, *257*, 1–11. [[CrossRef](#)]
67. Pan, Y.-W.; Hua, Y.; Zhou, S.; He, R.; Zhang, Y.; Yang, S.; Liu, X.; Lian, Y.; Yan, X.; Wu, B. A computational multi-node electro-thermal model for large prismatic lithium-ion batteries. *J. Power Sources* **2020**, *459*, 228070. [[CrossRef](#)]
68. Liang, J.; Gan, Y.; Yao, M.; Li, Y. Numerical analysis of capacity fading for a LiFePO₄ battery under different current rates and ambient temperatures. *Int. J. Heat Mass Transf.* **2020**, *165*, 120615. [[CrossRef](#)]
69. Richardson, R.R.; Ireland, P.T.; Howey, D. Battery internal temperature estimation by combined impedance and surface temperature measurement. *J. Power Sources* **2014**, *265*, 254–261. [[CrossRef](#)]
70. Kolodziejczyk, F.; Mortazavi, B.; Rabczuk, T.; Zhuang, X. Machine learning assisted multiscale modeling of composite phase change materials for Li-ion batteries' thermal management. *Int. J. Heat Mass Transf.* **2021**, *172*, 121199. [[CrossRef](#)]
71. Wen, J.; Zou, Q.; Wei, Y. Physics-driven machine learning model on temperature and time-dependent deformation in lithium metal and its finite element implementation. *J. Mech. Phys. Solids* **2021**, *153*, 104481. [[CrossRef](#)]
72. Deng, Z.; Hu, X.; Lin, X.; Che, Y.; Xu, L.; Guo, W. Data-driven state of charge estimation for lithium-ion battery packs based on Gaussian process regression. *Energy* **2020**, *205*, 118000. [[CrossRef](#)]
73. Li, W.; Garg, A.; Xiao, M.; Gao, L. Optimization for Liquid Cooling Cylindrical Battery Thermal Management System Based on Gaussian Process Model. *J. Therm. Sci. Eng. Appl.* **2020**, *13*, 1–19. [[CrossRef](#)]
74. Feng, F.; Teng, S.; Liu, K.; Xie, J.; Xie, Y.; Liu, B.; Li, K. Co-estimation of lithium-ion battery state of charge and state of temperature based on a hybrid electrochemical-thermal-neural-network model. *J. Power Sources* **2020**, *455*, 227935. [[CrossRef](#)]
75. Kleiner, J.; Stuckenberger, M.; Komsysiaka, L.; Endisch, C. Advanced Monitoring and Prediction of the Thermal State of Intelligent Battery Cells in Electric Vehicles by Physics-Based and Data-Driven Modeling. *Batteries* **2021**, *7*, 31. [[CrossRef](#)]
76. Hu, X.; Lin, S.; Stanton, S.; Lian, W. A Foster Network Thermal Model for HEV/EV Battery Modeling. *IEEE Trans. Ind. Appl.* **2011**, *47*, 1692–1699. [[CrossRef](#)]
77. Solai, E.; Guadagnini, M.; Beaugendre, H.; Daccord, R.; Congedo, P. Validation of a data-driven fast numerical model to simulate the immersion cooling of a lithium-ion battery pack. *Energy* **2022**, *249*, 123633. [[CrossRef](#)]
78. Kong, L.; Khan, M.K.; Wu, F.; Chen, G.; Zeng, P. Millimeter-Wave Wireless Communications for IoT-Cloud Supported Autonomous Vehicles: Overview, Design, and Challenges. *IEEE Commun. Mag.* **2017**, *55*, 62–68. [[CrossRef](#)]
79. Bellotti, F.; Berta, R.; Kobeissi, A.; Osman, N.; Arnold, E.; Dianati, M.; Nagy, B.; Gloria, A.D. Designing an IoT Framework for Automated Driving Impact Analysis. In Proceedings of the 2019 IEEE Intelligent Vehicles Symposium (IV), Paris, France, 9–12 June 2019; pp. 1111–1117.
80. Celesti, A.; Galletta, A.; Carnevale, L.; Fazio, M.; Lay-Ekuakille, A.; Villari, M. An IoT Cloud System for Traffic Monitoring and Vehicular Accidents Prevention Based on Mobile Sensor Data Processing. *IEEE Sens. J.* **2017**, *18*, 4795–4802. [[CrossRef](#)]
81. Kobeissi, A.H.; Bellotti, F.; Berta, R.; Gloria, A.D. IoT Grid Alignment Assistant System for Dynamic Wireless Charging of Electric Vehicles. In Proceedings of the 2018 Fifth International Conference on Internet of Things: Systems, Management and Security, Valencia, Spain, 15–18 October 2018; pp. 274–279.
82. Tran, M.-K.; Panchal, S.; Khang, T.D.; Panchal, K.; Fraser, R.; Fowler, M. Concept Review of a Cloud-Based Smart Battery Management System for Lithium-Ion Batteries: Feasibility, Logistics, and Functionality. *Batteries* **2022**, *8*, 19. [[CrossRef](#)]
83. Kim, Y.; Oh, H.; Kang, S. Proof of Concept of Home IoT Connected Vehicles. *Sensors* **2017**, *17*, 1289. [[CrossRef](#)] [[PubMed](#)]
84. Shabani, B.; Biju, M. Theoretical Modelling Methods for Thermal Management of Batteries. *Energies* **2015**, *8*, 10153–10177. [[CrossRef](#)]
85. Pesaran, A.A.; Burch, S.; Keyser, M. An Approach for Designing Thermal Management Systems for Electric and Hybrid Vehicle Battery Packs. In Proceedings of the Fourth Vehicle Thermal Management Systems Conference and Exhibition, London, UK, 24–27 May 1999.
86. Wang, T.; Tseng, K.; Zhao, J.; Wei, Z. Thermal investigation of lithium-ion battery module with different cell arrangement structures and forced air-cooling strategies. *Appl. Energy* **2014**, *134*, 229–238. [[CrossRef](#)]
87. Yang, N.; Zhang, X.; Li, G.; Hua, D. Assessment of the forced air-cooling performance for cylindrical lithium-ion battery packs: A comparative analysis between aligned and staggered cell arrangements. *Appl. Therm. Eng.* **2015**, *80*, 55–65. [[CrossRef](#)]
88. Yang, T.; Yang, N.; Zhang, X.; Li, G. Investigation of the thermal performance of axial-flow air cooling for the lithium-ion battery pack. *Int. J. Therm. Sci.* **2016**, *108*, 132–144. [[CrossRef](#)]

89. Afzal, A.; Samee, A.D.M.; Razak, R.K.A.; Ramis, M.K. Effect of spacing on thermal performance characteristics of Li-ion battery cells. *J. Therm. Anal.* **2018**, *135*, 1797–1811. [[CrossRef](#)]
90. Afzal, A.; Mujeebu, M.A. Thermo-Mechanical and Structural Performances of Automobile Disc Brakes: A Review of Numerical and Experimental Studies. *Arch. Comput. Methods Eng.* **2018**, *26*, 1489–1513. [[CrossRef](#)]
91. Park, S.; Jung, D. Battery cell arrangement and heat transfer fluid effects on the parasitic power consumption and the cell temperature distribution in a hybrid electric vehicle. *J. Power Sources* **2013**, *227*, 191–198. [[CrossRef](#)]
92. Sun, H.; Dixon, R. Development of cooling strategy for an air cooled lithium-ion battery pack. *J. Power Sources* **2014**, *272*, 404–414. [[CrossRef](#)]
93. Chen, K.; Wang, S.; Song, M.; Chen, L. Structure optimization of parallel air-cooled battery thermal management system. *Int. J. Heat Mass Transf.* **2017**, *111*, 943–952. [[CrossRef](#)]
94. Jiaqiang, E.; Yue, M.; Chen, J.; Zhu, H.; Deng, Y.; Zhu, Y.; Zhang, F.; Wen, M.; Zhang, B.; Kang, S. Effects of the different air cooling strategies on cooling performance of a lithium-ion battery module with baffle. *Appl. Therm. Eng.* **2018**, *144*, 231–241. [[CrossRef](#)]
95. Shahid, S.; Agelin-Chaab, M. Development and analysis of a technique to improve air-cooling and temperature uniformity in a battery pack for cylindrical batteries. *Therm. Sci. Eng. Prog.* **2018**, *5*, 351–363. [[CrossRef](#)]
96. Hong, S.; Zhang, X.; Chen, K.; Wang, S. Design of flow configuration for parallel air-cooled battery thermal management system with secondary vent. *Int. J. Heat Mass Transf.* **2018**, *116*, 1204–1212. [[CrossRef](#)]
97. Zhao, G.; Wang, X.; Negnevitsky, M.; Zhang, H. A review of air-cooling battery thermal management systems for electric and hybrid electric vehicles. *J. Power Sources* **2021**, *501*, 230001. [[CrossRef](#)]
98. Behi, H.; Karimi, D.; Behi, M.; Ghanbarpour, M.; Jaguemont, J.; Sokkeh, M.A.; Gandoman, F.H.; Berecibar, M.; Van Mierlo, J. A new concept of thermal management system in Li-ion battery using air cooling and heat pipe for electric vehicles. *Appl. Therm. Eng.* **2020**, *174*, 115280. [[CrossRef](#)]
99. Yi, J.; Koo, B.; Shin, C.B.; Han, T.; Park, S. Modeling the effect of aging on the electrical and thermal behaviors of a lithium-ion battery during constant current charge and discharge cycling. *Comput. Chem. Eng.* **2017**, *99*, 31–39. [[CrossRef](#)]
100. Cho, G.Y.; Choi, J.W.; Park, J.H.; Cha, S.W. Transient modeling and validation of lithium ion battery pack with air cooled thermal management system for electric vehicles. *Int. J. Automot. Technol.* **2014**, *15*, 795–803. [[CrossRef](#)]
101. Fan, Y.; Bao, Y.; Ling, C.; Chu, Y.; Tan, X.; Yang, S. Experimental study on the thermal management performance of air cooling for high energy density cylindrical lithium-ion batteries. *Appl. Therm. Eng.* **2019**, *155*, 96–109. [[CrossRef](#)]
102. Liu, Y.; Zhang, J. Design a J-type air-based battery thermal management system through surrogate-based optimization. *Appl. Energy* **2019**, *252*, 113426. [[CrossRef](#)]
103. He, H.; Jia, H.; Huo, W.; Sun, F. Field Synergy Analysis and Optimization of the Thermal Behavior of Lithium Ion Battery Packs. *Energies* **2017**, *10*, 81. [[CrossRef](#)]
104. Xu, X.; He, R. Research on the heat dissipation performance of battery pack based on forced air cooling. *J. Power Sources* **2013**, *240*, 33–41. [[CrossRef](#)]
105. Wang, T.; Tseng, K.; Zhao, J. Development of efficient air-cooling strategies for lithium-ion battery module based on empirical heat source model. *Appl. Therm. Eng.* **2015**, *90*, 521–529. [[CrossRef](#)]
106. Saw, B.; Ye, Y.; Tay, A.A.; Chong, W.T.; Kuan, S.H.; Yew, M.C. Computational fluid dynamic and thermal analysis of Lithium-ion battery pack with air cooling. *Appl. Energy* **2016**, *177*, 783–792. [[CrossRef](#)]
107. Erb, D.; Kumar, S.; Carlson, E.; Ehrenberg, I.; Sarma, S. Analytical methods for determining the effects of lithium-ion cell size in aligned air-cooled battery packs. *J. Energy Storage* **2017**, *10*, 39–47. [[CrossRef](#)]
108. Shahid, S.; Agelin-Chaab, M. Experimental and numerical studies on air cooling and temperature uniformity in a battery pack. *Int. J. Energy Res.* **2018**, *42*, 2246–2262. [[CrossRef](#)]
109. Na, X.; Kang, H.; Wang, T.; Wang, Y. Reverse layered air flow for Li-ion battery thermal management. *Appl. Therm. Eng.* **2018**, *143*, 257–262. [[CrossRef](#)]
110. Chen, K.; Song, M.; Wei, W.; Wang, S. Design of the structure of battery pack in parallel air-cooled battery thermal management system for cooling efficiency improvement. *Int. J. Heat Mass Transf.* **2019**, *132*, 309–321. [[CrossRef](#)]
111. Peng, X.; Ma, C.; Garg, A.; Bao, N.; Liao, X. Thermal performance investigation of an air-cooled lithium-ion battery pack considering the inconsistency of battery cells. *Appl. Therm. Eng.* **2019**, *153*, 596–603. [[CrossRef](#)]
112. He, F.; Ma, L. Thermal management of batteries employing active temperature control and reciprocating cooling flow. *Int. J. Heat Mass Transf.* **2015**, *83*, 164–172. [[CrossRef](#)]
113. Panchal, S.; Khasow, R.; Dincer, I.; Agelin-Chaab, M.; Fraser, R.; Fowler, M. Thermal design and simulation of mini-channel cold plate for water cooled large sized prismatic lithium-ion battery. *Appl. Therm. Eng.* **2017**, *122*, 80–90. [[CrossRef](#)]
114. Du, X.; Qian, Z.; Chen, Z.; Rao, Z. Experimental investigation on mini-channel cooling-based thermal management for Li-ion battery module under different cooling schemes. *Int. J. Energy Res.* **2018**, *42*, 2781–2788. [[CrossRef](#)]
115. Zhao, J.; Rao, Z.; Li, Y. Thermal performance of mini-channel liquid cooled cylinder based battery thermal management for cylindrical lithium-ion power battery. *Energy Convers. Manag.* **2015**, *103*, 157–165. [[CrossRef](#)]
116. Thakur, A.K.; Prabakaran, R.; Elkadeem, M.; Sharshir, S.W.; Arici, M.; Wang, C.; Zhao, W.; Hwang, J.-Y.; Saidur, R. A state of art review and future viewpoint on advance cooling techniques for Lithium-ion battery system of electric vehicles. *J. Energy Storage* **2020**, *32*, 101771. [[CrossRef](#)]

117. Al-Zareer, M.; Dincer, I.; Rosen, M.A. A novel approach for performance improvement of liquid to vapor based battery cooling systems. *Energy Convers. Manag.* **2019**, *187*, 191–204. [[CrossRef](#)]
118. Huo, Y.; Rao, Z. The numerical investigation of nanofluid based cylinder battery thermal management using lattice Boltzmann method. *Int. J. Heat Mass Transf.* **2015**, *91*, 374–384. [[CrossRef](#)]
119. Jilte, R.; Afzal, A.; Panchal, S. A novel battery thermal management system using nano-enhanced phase change materials. *Energy* **2020**, *219*, 119564. [[CrossRef](#)]
120. Yang, X.-H.; Tan, S.-C.; Liu, J. Thermal management of Li-ion battery with liquid metal. *Energy Convers. Manag.* **2016**, *117*, 577–585. [[CrossRef](#)]
121. Liu, Z.; Wang, H.; Yang, C.; Zhao, J. Simulation study of lithium-ion battery thermal management system based on a variable flow velocity method with liquid metal. *Appl. Therm. Eng.* **2020**, *179*, 115578. [[CrossRef](#)]
122. Yu, X.; Zhou, B.; Sobiesiak, A. Water and thermal management for Ballard PEM fuel cell stack. *J. Power Sources* **2005**, *147*, 184–195. [[CrossRef](#)]
123. Jarret, A.; Kim, I.Y. Design optimization of electric vehicle battery cooling plates for thermal performance. *J. Power Sources* **2011**, *196*, 10359–10368. [[CrossRef](#)]
124. Jarrett, A.; Kim, I.Y. Influence of operating conditions on the optimum design of electric vehicle battery cooling plates. *J. Power Sources* **2014**, *245*, 644–655. [[CrossRef](#)]
125. Hung, Y.-H.; Chen, J.-H.; Teng, T.-P. Feasibility Assessment of Thermal Management System for Green Power Sources Using Nanofluid. *J. Nanomater.* **2013**, *2013*, 1–11. [[CrossRef](#)]
126. Bandhauer, T.M.; Garimella, S. Passive, internal thermal management system for batteries using microscale liquid–vapor phase change. *Appl. Therm. Eng.* **2013**, *61*, 756–769. [[CrossRef](#)]
127. Lan, C.; Xu, J.; Qiao, Y.; Ma, Y. Thermal management for high power lithium-ion battery by minichannel aluminum tubes. *Appl. Therm. Eng.* **2016**, *101*, 284–292. [[CrossRef](#)]
128. Nieto, N.; Díaz, L.; Gastelurrutia, J.; Blanco, F.; Ramos, J.C.; Rivas, A. Novel thermal management system design methodology for power lithium-ion battery. *J. Power Sources* **2014**, *272*, 291–302. [[CrossRef](#)]
129. Qian, Z.; Li, Y.; Rao, Z. Thermal performance of lithium-ion battery thermal management system by using mini-channel cooling. *Energy Convers. Manag.* **2016**, *126*, 622–631. [[CrossRef](#)]
130. Zhang, S.; Zhao, R.; Liu, J.; Gu, J. Investigation on a hydrogel based passive thermal management system for lithium ion batteries. *Energy* **2014**, *68*, 854–861. [[CrossRef](#)]
131. Jin, L.; Lee, P.; Kong, X.; Fan, Y.; Chou, S. Ultra-thin minichannel LCP for EV battery thermal management. *Appl. Energy* **2013**, *113*, 1786–1794. [[CrossRef](#)]
132. Tong, W.; Somasundaram, K.; Birgersson, E.; Mujumdar, A.S.; Yap, C. Numerical investigation of water cooling for a lithium-ion bipolar battery pack. *Int. J. Therm. Sci.* **2015**, *94*, 259–269. [[CrossRef](#)]
133. Huo, Y.; Rao, Z.; Liu, X.; Zhao, J. Investigation of power battery thermal management by using mini-channel cold plate. *Energy Convers. Manag.* **2015**, *89*, 387–395. [[CrossRef](#)]
134. Saw, L.H.; Tay, A.A.O.; Zhang, L.W. Thermal management of lithium-ion battery pack with liquid cooling. In Proceedings of the 2015 31st Thermal Measurement, Modeling & Management Symposium (SEMI-THERM), San Jose, CA, USA, 15–19 March 2015; pp. 298–302. [[CrossRef](#)]
135. Smith, J.; Hinterberger, M.; Schneider, C.; Koehler, J. Energy savings and increased electric vehicle range through improved battery thermal management. *Appl. Therm. Eng.* **2016**, *101*, 647–656. [[CrossRef](#)]
136. Chen, D.; Jiang, J.; Kim, G.-H.; Yang, C.; Pesaran, A. Comparison of different cooling methods for lithium ion battery cells. *Appl. Therm. Eng.* **2016**, *94*, 846–854. [[CrossRef](#)]
137. Basu, S.; Hariharan, K.S.; Kolake, S.M.; Song, T.; Sohn, D.K.; Yeo, T. Coupled electrochemical thermal modelling of a novel Li-ion battery pack thermal management system. *Appl. Energy* **2016**, *181*, 1–13. [[CrossRef](#)]
138. Mondal, B.; Lopez, C.F.; Mukherjee, P.P. Exploring the efficacy of nanofluids for lithium-ion battery thermal management. *Int. J. Heat Mass Transf.* **2017**, *112*, 779–794. [[CrossRef](#)]
139. An, Z.; Jia, L.; Li, X.; Ding, Y. Experimental investigation on lithium-ion battery thermal management based on flow boiling in mini-channel. *Appl. Therm. Eng.* **2017**, *117*, 534–543. [[CrossRef](#)]
140. Gao, R.; Fan, Z.; Liu, S. A gradient channel-based novel design of liquid-cooled battery thermal management system for thermal uniformity improvement. *J. Energy Storage* **2022**, *48*, 104014. [[CrossRef](#)]
141. Khateeb, S.A.; Amiruddin, S.; Farid, M.; Selman, J.R.; Al-Hallaj, S. Thermal management of Li-ion battery with phase change material for electric scooters: Experimental validation. *J. Power Sources* **2005**, *142*, 345–353. [[CrossRef](#)]
142. Khateeb, S.A.; Farid, M.M.; Selman, J.R.; Al-Hallaj, S. Design and simulation of a lithium-ion battery with a phase change material thermal management system for an electric scooter. *J. Power Sources* **2004**, *128*, 292–307. [[CrossRef](#)]
143. Al Hallaj, S.; Selman, J.R. Novel thermal management system for electric vehicle batteries using phase-change material. *J. Electrochem. Soc.* **2000**, *147*, 3231–3236. [[CrossRef](#)]
144. Qu, Z.; Li, W.; Tao, W. Numerical model of the passive thermal management system for high-power lithium ion battery by using porous metal foam saturated with phase change material. *Int. J. Hydrogen Energy* **2014**, *39*, 3904–3913. [[CrossRef](#)]
145. Li, W.; Qu, Z.; He, Y.; Tao, Y. Experimental study of a passive thermal management system for high-powered lithium ion batteries using porous metal foam saturated with phase change materials. *J. Power Sources* **2014**, *255*, 9–15. [[CrossRef](#)]

146. Javani, N.; Dincer, I.; Naterer, G.; Rohrauer, G. Modeling of passive thermal management for electric vehicle battery packs with PCM between cells. *Appl. Therm. Eng.* **2014**, *73*, 307–316. [[CrossRef](#)]
147. Hémerly, C.-V.; Pra, F.; Robin, J.-F.; Marty, P. Experimental performances of a battery thermal management system using a phase change material. *J. Power Sources* **2014**, *270*, 349–358. [[CrossRef](#)]
148. Ling, Z.; Chen, J.; Fang, X.; Zhang, Z.; Xu, T.; Gao, X.; Wang, S. Experimental and numerical investigation of the application of phase change materials in a simulative power batteries thermal management system. *Appl. Energy* **2014**, *121*, 104–113. [[CrossRef](#)]
149. Wang, Z.; Zhang, Z.; Jia, L.; Yang, L. Paraffin and paraffin/aluminum foam composite phase change material heat storage experimental study based on thermal management of Li-ion battery. *Appl. Therm. Eng.* **2015**, *78*, 428–436. [[CrossRef](#)]
150. Babapoor, A.; Azizi, M.; Karimi, G. Thermal management of a Li-ion battery using carbon fiber-PCM composites. *Appl. Therm. Eng.* **2015**, *82*, 281–290. [[CrossRef](#)]
151. Shirazi, A.H.N.; Mohebbi, F.; Kakavand, M.R.A.; He, B.; Rabczuk, T. Paraffin Nanocomposites for Heat Management of Lithium-Ion Batteries: A Computational Investigation. *J. Nanomater.* **2016**, *2016*, 1–10. [[CrossRef](#)]
152. Rao, Z.; Wang, Q.; Huang, C.-L. Investigation of the thermal performance of phase change material/mini-channel coupled battery thermal management system. *Appl. Energy* **2016**, *164*, 659–669. [[CrossRef](#)]
153. Yang, Y.; Kuang, J.; Wang, H.; Song, G.; Liu, Y.; Tang, G. Enhancement in thermal property of phase change microcapsules with modified silicon nitride for solar energy. *Sol. Energy Mater. Sol. Cells* **2016**, *151*, 89–95. [[CrossRef](#)]
154. Sun, Z.; Fan, R.; Yan, F.; Zhou, T.; Zheng, N. Thermal management of the lithium-ion battery by the composite PCM-Fin structures. *Int. J. Heat Mass Transf.* **2019**, *145*, 118739. [[CrossRef](#)]
155. Hussain, A.; Tso, C.Y.; Chao, Y.H.C. Experimental investigation of a passive thermal management system for high-powered lithium ion batteries using nickel foam-paraffin composite. *Energy* **2016**, *115*, 209–218. [[CrossRef](#)]
156. Alipanah, M.; Li, X. Numerical studies of lithium-ion battery thermal management systems using phase change materials and metal foams. *Int. J. Heat Mass Transf.* **2016**, *102*, 1159–1168. [[CrossRef](#)]
157. Karimi, G.; Azizi, M.; Babapoor, A. Experimental study of a cylindrical lithium ion battery thermal management using phase change material composites. *J. Energy Storage* **2016**, *8*, 168–174. [[CrossRef](#)]
158. Samimi, F.; Babapoor, A.; Azizi, M.; Karimi, G. Thermal management analysis of a Li-ion battery cell using phase change material loaded with carbon fibers. *Energy* **2016**, *96*, 355–371. [[CrossRef](#)]
159. Malik, M.; Dincer, I.; Rosen, M.A. Review on use of phase change materials in battery thermal management for electric and hybrid electric vehicles. *Int. J. Energy Res.* **2016**, *40*, 1011–1031. [[CrossRef](#)]
160. Jiang, G.; Huang, J.; Fu, Y.; Cao, M.; Liu, M. Thermal optimization of composite phase change material/expanded graphite for Li-ion battery thermal management. *Appl. Therm. Eng.* **2016**, *108*, 1119–1125. [[CrossRef](#)]
161. Lv, Y.; Yang, X.; Li, X.; Zhang, G.; Wang, Z.; Yang, C. Experimental study on a novel battery thermal management technology based on low density polyethylene-enhanced composite phase change materials coupled with low fins. *Appl. Energy* **2016**, *178*, 376–382. [[CrossRef](#)]
162. Wu, W.; Yang, X.; Zhang, G.; Ke, X.; Wang, Z.; Situ, W.; Li, X.; Zhang, J. An experimental study of thermal management system using copper mesh-enhanced composite phase change materials for power battery pack. *Energy* **2016**, *113*, 909–916. [[CrossRef](#)]
163. Azizi, Y.; Sadrameli, S. Thermal management of a LiFePO₄ battery pack at high temperature environment using a composite of phase change materials and aluminum wire mesh plates. *Energy Convers. Manag.* **2016**, *128*, 294–302. [[CrossRef](#)]
164. Wu, W.; Yang, X.; Zhang, G.; Chen, K.; Wang, S. Experimental investigation on the thermal performance of heat pipe-assisted phase change material based battery thermal management system. *Energy Convers. Manag.* **2017**, *138*, 486–492. [[CrossRef](#)]
165. Hao, M.; Li, J.; Park, S.; Moura, S.; Dames, C. Efficient thermal management of Li-ion batteries with a passive interfacial thermal regulator based on a shape memory alloy. *Nat. Energy* **2018**, *3*, 899–906. [[CrossRef](#)]
166. Rodrigues, M.-T.F.; Babu, G.; Gullapalli, H.; Kalaga, K.; Sayed, F.N.; Kato, K.; Joyner, J.; Ajayan, P.M. A materials perspective on Li-ion batteries at extreme temperatures. *Nat. Energy* **2017**, *2*, 1–14. [[CrossRef](#)]
167. Wang, C.-Y.; Zhang, G.; Ge, S.; Xu, T.; Ji, Y.; Yang, X.-G.; Leng, Y. Lithium-ion battery structure that self-heats at low temperatures. *Nature* **2016**, *529*, 515–518. [[CrossRef](#)] [[PubMed](#)]
168. Zhang, S.; Xu, K.; Jow, T. A new approach toward improved low temperature performance of Li-ion battery. *Electrochem. Commun.* **2002**, *4*, 928–932. [[CrossRef](#)]
169. Vlahinos, A.; Pesaran, A.A. Energy Efficient Battery Heating in Cold Climates. *SAE Trans.* **2002**, *111*, 826–833. [[CrossRef](#)]
170. Viswanathan, V.V.; Choi, D.; Wang, D.; Xu, W.; Towne, S.; Williford, R.E.; Zhang, J.-G.; Liu, J.; Yang, Z. Effect of entropy change of lithium intercalation in cathodes and anodes on Li-ion battery thermal management. *J. Power Sources* **2010**, *195*, 3720–3729. [[CrossRef](#)]
171. Fleckenstein, M.; Bohlen, O.; Roscher, M.A.; Bäker, B. Current density and state of charge inhomogeneities in Li-ion battery cells with LiFePO₄ as cathode material due to temperature gradients. *J. Power Sources* **2011**, *196*, 4769–4778. [[CrossRef](#)]
172. Ning, G.; Haran, B.; Popov, B.N. Capacity fade study of lithium-ion batteries cycled at high discharge rates. *J. Power Sources* **2003**, *117*, 160–169. [[CrossRef](#)]
173. Doughty, D.H.; Roth, E.P. A General Discussion of Li Ion Battery Safety. *Electrochem. Soc. Interface* **2012**, *21*, 37–44. [[CrossRef](#)]
174. Shi, T.; Dong, Y.; Wang, C.-M.; Tao, F.; Chen, L. Enhanced cycle stability at high rate and excellent high rate capability of La_{0.7}Sr_{0.3}Mn_{0.7}Co_{0.3}O₃-coated LiMn₂O₄. *J. Power Sources* **2014**, *273*, 959–965. [[CrossRef](#)]

175. Zhao, R.; Zhang, S.; Liu, J.; Gu, J. A review of thermal performance improving methods of lithium ion battery: Electrode modification and thermal management system. *J. Power Sources* **2015**, *299*, 557–577. [[CrossRef](#)]
176. Loges, A.; Herberger, S.; Seegert, P.; Wetzel, T. A study on specific heat capacities of Li-ion cell components and their influence on thermal management. *J. Power Sources* **2016**, *336*, 341–350. [[CrossRef](#)]
177. Yang, X.-G.; Zhang, G.; Ge, S.; Wang, C.-Y. Fast charging of lithium-ion batteries at all temperatures. *Proc. Natl. Acad. Sci. USA* **2018**, *115*, 7266–7271. [[CrossRef](#)]
178. Huang, Y.; Tang, Y.; Yuan, W.; Fang, G.; Yang, Y.; Zhang, X.; Wu, Y.; Yuan, Y.; Wang, C.; Li, J. Challenges and recent progress in thermal management with heat pipes for lithium-ion power batteries in electric vehicles. *Sci. China Technol. Sci.* **2021**, *64*, 919–956. [[CrossRef](#)]
179. Lee, G.G.; Choi, Y.H.; Park, C. Heat Managing Unit of High Voltage Battery. U.S. Patent 9,350,056, 24 May 2016.
180. Smith, J.; Singh, R.; Hinterberger, M.; Mochizuki, M. Battery thermal management system for electric vehicle using heat pipes. *Int. J. Therm. Sci.* **2018**, *134*, 517–529. [[CrossRef](#)]
181. Greco, A.; Cao, D.; Jiang, X.; Yang, H. A theoretical and computational study of lithium-ion battery thermal management for electric vehicles using heat pipes. *J. Power Sources* **2014**, *257*, 344–355. [[CrossRef](#)]
182. Zhang, Z.; Wei, K. Experimental and numerical study of a passive thermal management system using flat heat pipes for lithium-ion batteries. *Appl. Therm. Eng.* **2020**, *166*, 114660. [[CrossRef](#)]
183. Gan, Y.; He, L.; Liang, J.; Tan, M.; Xiong, T.; Li, Y. A numerical study on the performance of a thermal management system for a battery pack with cylindrical cells based on heat pipes. *Appl. Therm. Eng.* **2020**, *179*, 115740. [[CrossRef](#)]
184. Qu, J.; Wang, C.; Li, X.; Wang, H. Heat transfer performance of flexible oscillating heat pipes for electric/hybrid-electric vehicle battery thermal management. *Appl. Therm. Eng.* **2018**, *135*, 1–9. [[CrossRef](#)]
185. Rao, Z.; Wang, S.; Wu, M.; Lin, Z.; Li, F. Experimental investigation on thermal management of electric vehicle battery with heat pipe. *Energy Convers. Manag.* **2013**, *65*, 92–97. [[CrossRef](#)]
186. Li, Y.; Guo, H.; Qi, F.; Guo, Z.; Li, M.; Tjernberg, L.B. Investigation on liquid cold plate thermal management system with heat pipes for LiFePO₄ battery pack in electric vehicles. *Appl. Therm. Eng.* **2020**, *185*, 116382. [[CrossRef](#)]
187. Mbulu, H.; Laounual, Y.; Wongwises, S. Experimental study on the thermal performance of a battery thermal management system using heat pipes. *Case Stud. Therm. Eng.* **2021**, *26*, 101029. [[CrossRef](#)]
188. Nasir, F.M.; Abdullah, M.Z.; Ismail, M.A. Experimental Investigation of Water-Cooled Heat Pipes in the Thermal Management of Lithium-Ion EV Batteries. *Arab. J. Sci. Eng.* **2019**, *44*, 7541–7552. [[CrossRef](#)]
189. Wang, Q.; Jiang, B.; Xue, Q.; Sun, H.; Li, B.; Zou, H.; Yan, Y. Experimental investigation on EV battery cooling and heating by heat pipes. *Appl. Therm. Eng.* **2014**, *88*, 54–60. [[CrossRef](#)]
190. Putra, N.; Ariantara, B. Electric motor thermal management system using L-shaped flat heat pipes. *Appl. Therm. Eng.* **2017**, *126*, 1156–1163. [[CrossRef](#)]
191. Zhao, R.; Gu, J.; Liu, J. An experimental study of heat pipe thermal management system with wet cooling method for lithium ion batteries. *J. Power Sources* **2015**, *273*, 1089–1097. [[CrossRef](#)]
192. Wang, J.; Gan, Y.; Liang, J.; Tan, M.; Li, Y. Sensitivity analysis of factors influencing a heat pipe-based thermal management system for a battery module with cylindrical cells. *Appl. Therm. Eng.* **2019**, *151*, 475–485. [[CrossRef](#)]
193. Liang, J.; Gan, Y.; Li, Y. Investigation on the thermal performance of a battery thermal management system using heat pipe under different ambient temperatures. *Energy Convers. Manag.* **2018**, *155*, 1–9. [[CrossRef](#)]
194. Jiang, Z.; Qu, Z. Lithium-ion battery thermal management using heat pipe and phase change material during discharge-charge cycle: A comprehensive numerical study. *Appl. Energy* **2019**, *242*, 378–392. [[CrossRef](#)]
195. Tang, H.; Tang, Y.; Wan, Z.; Li, J.; Yuan, W.; Lu, L.; Li, Y.; Tang, K. Review of applications and developments of ultra-thin micro heat pipes for electronic cooling. *Appl. Energy* **2008**, *223*, 383–400. [[CrossRef](#)]
196. Jouhara, H.; Serey, N.; Khordehghah, N.; Bennett, R.; Almahmoud, S.; Lester, S.A.S.P. Investigation, development and experimental analyses of a heat pipe based battery thermal management system. *Int. J. Thermofluids* **2019**, *1–2*, 100004. [[CrossRef](#)]
197. Behi, H.; Behi, M.; Karimi, D.; Jaguemont, J.; Ghanbarpour, M.; Behnia, M.; Berecibar, M.; Van Mierlo, J. Heat pipe air-cooled thermal management system for lithium-ion batteries: High power applications. *Appl. Therm. Eng.* **2021**, *183*, 116240. [[CrossRef](#)]
198. Zhou, H.; Dai, C.; Liu, Y.; Fu, X.; Du, Y. Experimental investigation of battery thermal management and safety with heat pipe and immersion phase change liquid. *J. Power Sources* **2020**, *473*, 228545. [[CrossRef](#)]
199. Yao, M.; Gan, Y.; Liang, J.; Dong, D.; Ma, L.; Liu, J.; Luo, Q.; Li, Y. Performance simulation of a heat pipe and refrigerant-based lithium-ion battery thermal management system coupled with electric vehicle air-conditioning. *Appl. Therm. Eng.* **2021**, *191*, 116878. [[CrossRef](#)]
200. Chen, M.; Li, J. Nanofluid-based pulsating heat pipe for thermal management of lithium-ion batteries for electric vehicles. *J. Energy Storage* **2020**, *32*, 101715. [[CrossRef](#)]
201. Zhang, C.; Xia, Z.; Wang, B.; Gao, H.; Chen, S.; Zong, S.; Luo, K. A Li-Ion Battery Thermal Management System Combining a Heat Pipe and Thermoelectric Cooler. *Energies* **2020**, *13*, 841. [[CrossRef](#)]
202. Sakile, R.; Sinha, U.K. Estimation of Lithium-Ion Battery State of Charge for Electric Vehicles Using an Adaptive Joint Algorithm. *Adv. Theory Simul.* **2022**, *5*, 2100397. [[CrossRef](#)]
203. Hu, X.; Sun, F.; Zou, Y. Estimation of State of Charge of a Lithium-Ion Battery Pack for Electric Vehicles Using an Adaptive Luenberger Observer. *Energies* **2010**, *3*, 1586–1603. [[CrossRef](#)]

204. Cen, J.; Jiang, F. Li-ion power battery temperature control by a battery thermal management and vehicle cabin air conditioning integrated system. *Energy Sustain. Dev.* **2020**, *57*, 141–148. [[CrossRef](#)]
205. Buidin, T.; Mariasiu, F. Battery Thermal Management Systems: Current Status and Design Approach of Cooling Technologies. *Energies* **2021**, *14*, 4879. [[CrossRef](#)]
206. Xu, J.; Zhang, C.; Wan, Z.; Chen, X.; Chan, S.H.; Tu, Z. Progress and perspectives of integrated thermal management systems in PEM fuel cell vehicles: A review. *Renew. Sustain. Energy Rev.* **2021**, *155*, 111908. [[CrossRef](#)]
207. Tie, S.F.; Tan, C.W. A review of energy sources and energy management system in electric vehicles. *Renew. Sustain. Energy Rev.* **2013**, *20*, 82–102. [[CrossRef](#)]
208. Lukic, S.M.; Wirasingha, S.G.; Rodriguez, F.; Cao, J.; Emadi, A. Power Management of an Ultracapacitor/Battery Hybrid Energy Storage System in an HEV. In Proceedings of the IEEE Vehicle Power and Propulsion Conference, Windsor, UK, 6–8 September 2006; pp. 1–6.
209. Tan, K.M.; Ramachandaramurthy, V.K.; Yong, J.Y. Integration of electric vehicles in smart grid: A review on vehicle to grid technologies and optimization techniques. *Renew. Sustain. Energy Rev.* **2016**, *53*, 720–732. [[CrossRef](#)]
210. Ahmad, A.; Alam, M.S.; Chabaan, R. A Comprehensive Review of Wireless Charging Technologies for Electric Vehicles. *IEEE Trans. Transp. Electrification* **2017**, *4*, 38–63. [[CrossRef](#)]
211. Araújo, R.E.; De Castro, R.; Pinto, C.; Melo, P.; Freitas, D. Combined Sizing and Energy Management in EVs With Batteries and Supercapacitors. *IEEE Trans. Veh. Technol.* **2014**, *63*, 3062–3076. [[CrossRef](#)]
212. Patil, H.; Kalkhambkar, V.N. Grid Integration of Electric Vehicles for Economic Benefits: A Review. *J. Mod. Power Syst. Clean Energy* **2021**, *9*, 13–26. [[CrossRef](#)]
213. Arefifar, S.A.; Ordonez, M.; Ibrahim-Mohamed, Y. Energy Management in Multi-Microgrid Systems—Development and Assessment. *IEEE Trans. Power Syst.* **2016**, *32*, 1. [[CrossRef](#)]
214. Hung, Y.-H.; Wu, C.-H. A combined optimal sizing and energy management approach for hybrid in-wheel motors of EVs. *Appl. Energy* **2015**, *139*, 260–271. [[CrossRef](#)]
215. Zhang, R.; Cheng, X.; Yang, L. Flexible Energy Management Protocol for Cooperative EV-to-EV Charging. *IEEE Trans. Intell. Transp. Syst.* **2018**, *20*, 172–184. [[CrossRef](#)]
216. Van Der Meer, D.; Mouli, G.R.C.; Mouli, G.M.-E.; Elizondo, L.R.; Bauer, P. Energy Management System with PV Power Forecast to Optimally Charge EVs at the Workplace. *IEEE Trans. Ind. Inform.* **2016**, *14*, 311–320. [[CrossRef](#)]
217. Vatanparvar, K.; Faruque, M.A.A. OTEM: Optimized Thermal and Energy Management for Hybrid Electrical Energy Storage in Electric Vehicles. In Proceedings of the 2016 Design, Automation & Test in Europe Conference & Exhibition (DATE), Dresden, Germany, 14–18 March 2016; pp. 19–24.
218. Lescot, J.; Sciarretta, A.; Chamailard, Y.; Charlet, A. On the integration of optimal energy management and thermal management of hybrid electric vehicles. In Proceedings of the IEEE Vehicle Power and Propulsion Conference, Lille, France, 1–3 September 2010; pp. 1–6.
219. Shams-Zahraei, M.; Kouzani, A.Z.; Kutter, S.; Bäker, B. Integrated thermal and energy management of plug-in hybrid electric vehicles. *J. Power Sources* **2012**, *216*, 237–248. [[CrossRef](#)]
220. Zhang, L.; Yang, L.; Guo, X.; Yuan, X. Stage-by-phase multivariable combination control for centralized and distributed drive modes switching of electric vehicles. *Mech. Mach. Theory* **2020**, *147*, 103752. [[CrossRef](#)]
221. Wei, H.; Zhang, N.; Liang, J.; Ai, Q.; Zhao, W.; Huang, T.; Zhang, Y. Deep reinforcement learning based direct torque control strategy for distributed drive electric vehicles considering active safety and energy saving performance. *Energy* **2021**, *238*, 121725. [[CrossRef](#)]
222. Bogloul, V.; Karavas, C.; Karlis, A.; Arvanitis, K. An intelligent decentralized energy management strategy for the optimal electric vehicles' charging in low-voltage islanded microgrids. *Int. J. Energy Res.* **2021**, *46*, 2988–3016. [[CrossRef](#)]
223. Chen, W.; Wang, J.; Yu, G.; Chen, J.; Hu, Y. Research on day-ahead transactions between multi-microgrid based on cooperative game model. *Appl. Energy* **2022**, *316*, 119106. [[CrossRef](#)]